




# Anatomically segregated basal ganglia pathways allow parallel behavioral modulation

Jaeon Lee, Wengang Wang and Bernardo L. Sabatini  

**In the basal ganglia (BG), anatomically segregated and topographically organized feedforward circuits are thought to modulate multiple behaviors in parallel. Although topographically arranged BG circuits have been described, the extent to which these relationships are maintained across the BG output nuclei and in downstream targets is unclear. Here, using focal *trans*-synaptic anterograde tracing, we show that the motor-action-related topographical organization of the striatum is preserved in all BG output nuclei. The topography is also maintained downstream of the BG and in multiple parallel closed loops that provide striatal input. Furthermore, focal activation of two distinct striatal regions induces either licking or turning, consistent with their respective anatomical targets of projection outside of the BG. Our results confirm the parallel model of BG function and suggest that the integration and competition of information relating to different behavior occur largely outside of the BG.**

The BG are subcortical nuclei involved in decision making and motor control<sup>1–3</sup>. The striatum (STR), the main input region of the BG, sends projections to three output nuclei—the entopeduncular nucleus (EP), globus pallidus externus (GPe) and substantia nigra pars reticulata (SNr). These nuclei, in turn, project directly or indirectly to thalamus, superior colliculus (SC), brain stem (BS) and other regions to modulate behavior.

Two models of BG function predict radically different architectures and topographical organization of BG circuits and outputs. One model posits that BG circuits mediate learning of arbitrary stimulus–response associations<sup>4,5</sup>. In this model, stimulus identity is encoded in the input to striatum which activates specific striatal neurons that generate a specific behavior. If the behavior leads to a reward, dopamine is thought to reinforce that stimulus–response association<sup>6,7</sup>. In order for BG to be able to reinforce arbitrary stimulus–response associations, projections from striatum to BG output nuclei need to form an all-to-all connected network, allowing cross talk between each striatum pathway as necessary for contextual information to control any potential motor output. In contrast, a different model posits that each BG pathway controls only a specific set of behaviors<sup>8</sup>. In this model, each pathway remains anatomically segregated and innervates a unique set of target brain regions, endowing each BG pathway with exclusive control over specific aspects of behavior.

Anatomical evidence for both models exists. Studies in primates and rodents indicate that BG projections are topographically organized and subdivided into segregated anatomical pathways targeting different subsets of brain regions and premotor nuclei<sup>8–10</sup>. However, other evidence suggests that there is considerable convergence within the BG. Stimulation of distinct cortical regions that innervate distinct striatal subregions activates the same subthalamic or SNr neurons, suggesting nonparallel organization within the BG<sup>11,12</sup>. In vivo, optogenetic activation of the direct pathway in a striatal subregion (for example, DMS) can induce an array of different behaviors including locomotion, nose poke reinforcement, arm movement reinforcement and visual detection modulation in different tasks<sup>1,2,13–15</sup>. These studies support a model whereby a single BG pathway has access to an overlapping pool of premotor nuclei encoding different sets of actions. Thus, depending on the

behavioral context, stimulating the same striatal region reveals categorically different behavioral phenotypes, highlighting the diverse behavioral functions a single BG pathway can carry out.

One of the difficulties in interpreting some of these previous retrograde tracing experiments is the lack of specificity of the tracers. For instance, wild-type rabies virus does not specifically infect one projection. Given that striatum can target cortex via multiple routes (for example, striatum→GPe→cortex; striatum→subthalamus→cortex; striatum→SNr→thalamus→cortex), it may be difficult to determine, by solely using survival time of neurons after virus injection, which of these polysynaptic pathways is taken by cortically injected rabies<sup>16–19</sup>. On the other hand, one potential caveat in interpreting most gain-of-function optogenetic studies in rodent striatum is the lack of anatomical specificity of the stimulation. Optogenetic activation is generally done by delivering high-power light to a large volume widely expressing an activator protein (for example, ChR2)<sup>1,2,14,15,20</sup>. In this regime, the effects of stimulation may arise from the region immediately below the fiber tip (usually the reported location of effect) or from a more distant region that expresses the activator opsin and is exposed to light<sup>21,22</sup>. Given this caveat, it is possible that the many phenotypes observed by attempting to stimulate a single region of striatum might be a collection resulting from stimulating distinct and varying regions.

To avoid these caveats, we used a spatially targeted approach to reveal the anatomical organization of the BG and the behavioral consequences of focally activating striatum in the mouse. Using a combination of focal anterograde tracing, slice electrophysiology and spatially precise optogenetic manipulations in vivo, we show that the outputs of the BG are subdivided into anatomically and functionally segregated pathways. Anatomically, SNr projections to the parafascicular nucleus (PF), ventromedial thalamus (VM) and SC are topographically organized. These three nuclei, in turn, project back to the striatal region from which they receive input, suggesting the existence of at least three closed BG loops. Using tapered optical fibers to optogenetically activate focal regions of striatum, we reveal functional maps for licking and locomotor turning, arising from ventrolateral striatum (VLS) and ventromedial/dorsomedial striatum (VMS and DMS, or MS), respectively. These two distinct striatal regions, via SNr, have access to the relevant

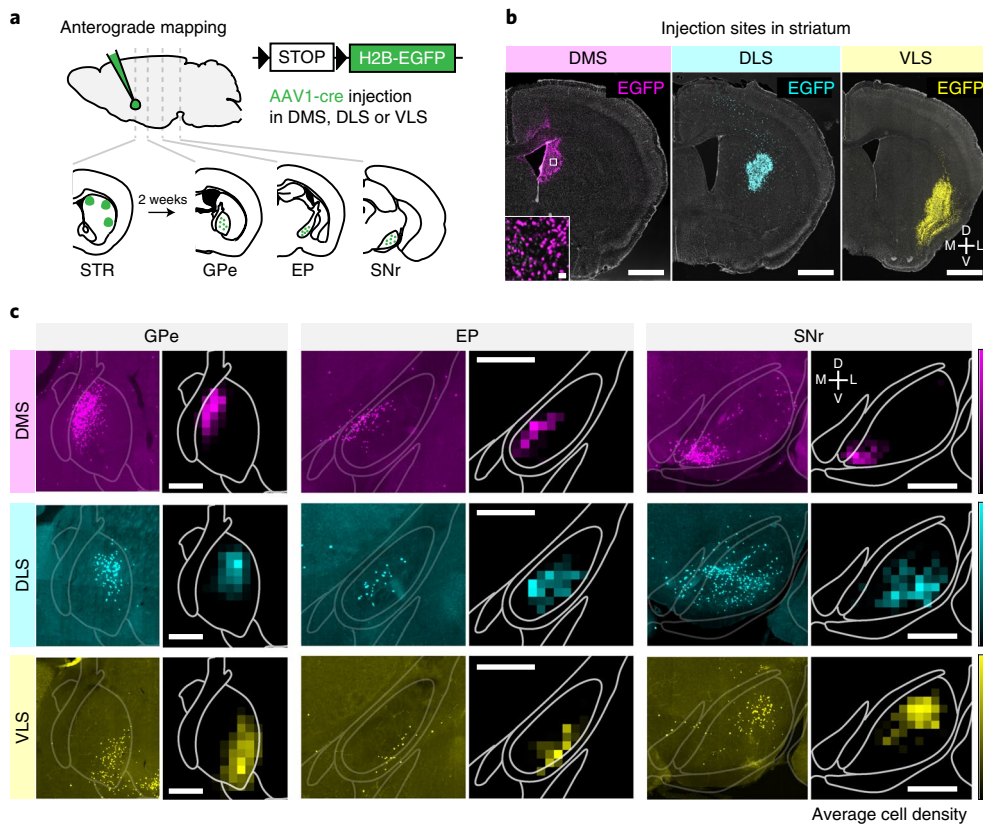


**Fig. 1 | Topographically organized projection from BG input to output nuclei.** **a**, Experimental protocol for studying topography in the BG. Top sagittal section: AAV1-Cre is injected into DMS, DLS or VLS of H2B-EGFP reporter mice. Bottom coronal sections: after 2 weeks, the Cre encoded by the virus activates H2B-EGFP expression at the injection site (STR) as well as, due to its anterograde propagation, in the BG output nuclei. **b**, Example coronal sections of striatum showing the injection sites (scale bar, 1 mm) with fluorescence of the H2B-EGFP shown in indicated colors: DMS (magenta), DLS (cyan) and VLS (yellow). Similar results were obtained in  $n = 9$  mice ( $n = 3$  for each site). **c**, Example coronal section (left column) and average relative cell density map of H2B-EGFP-expressing cells (right column) in GPe (left), EP (middle) and SNr (right) for injections at three different striatal sites as indicated (top, DMS; middle, DLS; bottom, VLS) ( $n = 3$  mice for each striatal injection site; scale bar, 500  $\mu\text{m}$ ). D, dorsal; L, lateral; M, medial; V, ventral.

cortical, collicular and brain stem regions involved in licking<sup>23,24</sup> and orienting<sup>25,26</sup>, respectively. Activation of VLS modulates the activity of cortical and collicular regions involved in licking, consistent with the existence of a functional lick-controlling loop involving BG. Stimulation of striatal regions outside of the VLS ‘lick zone’ did not interfere with the mouse’s ability to make correct lick decisions for reward, supporting a parallel organization of motor-related BG outputs. Our results support a model of BG in which multiple segregated pathways project to distinct anatomical regions to control specific behaviors in parallel.

## Results

**Topographical organization of projections from striatum to BG output nuclei.** We took advantage of the anterograde *trans*-synaptic property of the adeno-associated virus serotype 1 (AAV1) to investigate the topography of the BG circuitry<sup>27,28</sup>. Briefly, our strategy was to use a reporter mouse, *Rosa26-Lox-STOP-Lox-H2B-EGFP* (referred to as H2B-EGFP reporter mouse), and inject AAV1 encoding Cre recombinase (AAV1-Cre) into a region of interest. Two weeks later, AAV1-Cre had traveled anterograde, entering a subset of postsynaptic cells and activating reporter expression. Thus, imaging EGFP in downstream regions allowed easy identification of cells postsynaptic to the AAV1-Cre-infected ‘starter’ cells (Fig. 1a). We chose to examine three striatal regions that have been extensively studied—dosomedial striatum (DMS), dorsolateral striatum (DLS) and ventrolateral striatum (VLS). Previous studies

that subdivided striatum based on clustering of cortical inputs also identified DMS, DLS and VLS as distinct striatal compartments<sup>29–31</sup>. We injected AAV1-Cre into one striatal subregion of the H2B-EGFP reporter mouse to activate nuclear EGFP fluorescence on Cre expression. This resulted in labeled cells around the injection site and in downstream regions such as GPe, EP and SNr targeted by the axons of neurons at the injection site (Fig. 1b,c). We found that within GPe, EP and SNr, the location of anterogradely labeled cells depended on the location of the injection in striatum, indicating a topographical relationship between striatal subregions and output nuclei (Fig. 1c). Injections in multiple mice ( $n = 3$  per site) and calculation of the average cell density maps revealed a consistent pattern of projections to subregions within GPe, EP and SNr (Fig. 1c and Extended Data Fig. 1). Since the striatal direct pathway projects to all BG output nuclei, whereas the indirect pathway projects only to GPe, our results suggest that both pathways arising from DMS, DLS and VLS maintain topography to all three BG output nuclei.

**Trans-synaptic anterograde tracing reveals topography downstream of BG.** We examined whether the BG output projections remain segregated downstream of BG. We injected two AAV1s encoding different recombinases (Cre and Flpo) into medial and lateral striatum and then injected a mixture of AAVs, one that expresses a red fluorophore (tdTomato) in a Cre-dependent manner and one that expresses a green fluorophore (EYFP) in a

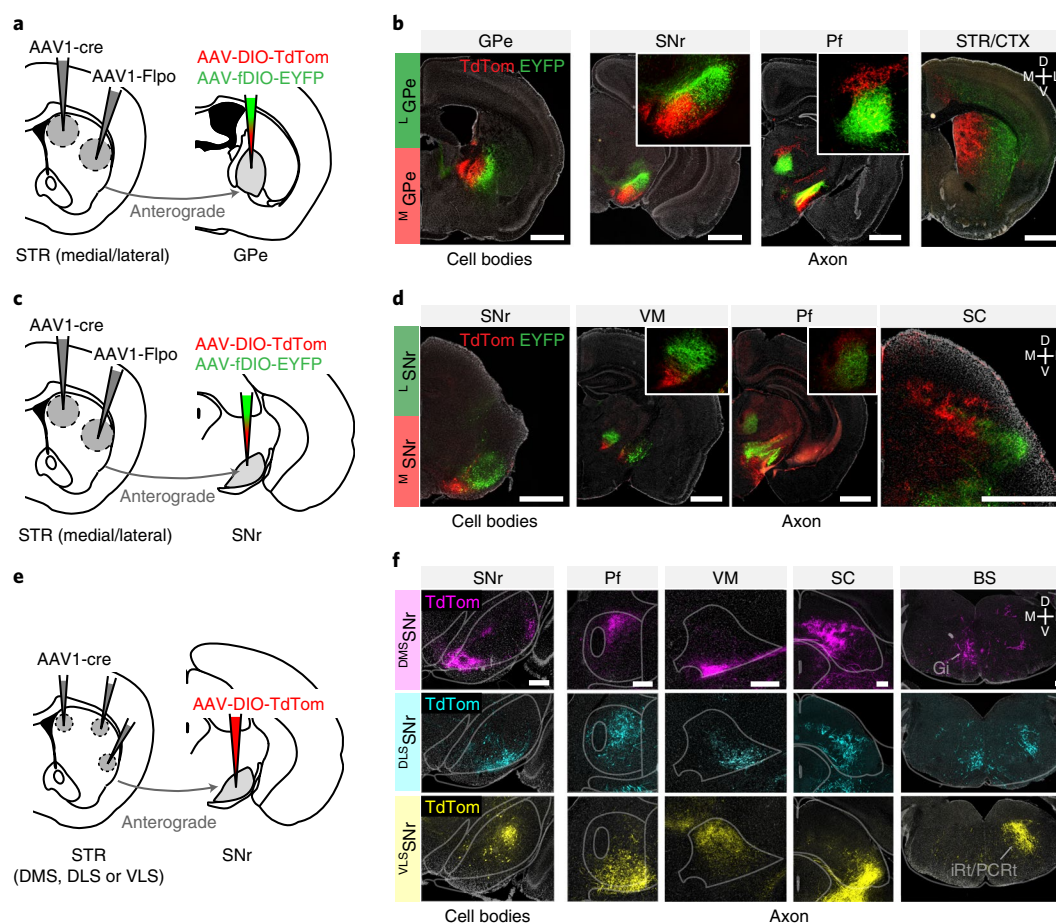


**Fig. 2 | Projections of BG output nuclei to downstream targets maintain segregated topography.** **a**, Protocol for tracing medial-lateral topography in GPe. AAV1-Cre and AAV1-Flpo were injected in the medial and lateral striatum, respectively, followed by injection in GPe of a mixture of AAVs encoding fluorophores whose expression is activated by either Cre (AAV-DIO-tdTom) or Flpo (AAV-fDIO-EYFP) recombinase. Anterograde movement of AAV1-Cre activates tdTom expression in the cells of the medial striatum target zone of the GPe (<sup>M</sup>GPe), whereas AAV1-Flpo activates EYFP expression in the lateral striatum target zone (<sup>L</sup>GPe). **b**, Example coronal sections showing fluorophore-expressing cell bodies in GPe (left) and their labeled axons downstream of the GPe (right three panels) in SNr, Pf and striatum/cortex (STR/CTX), as indicated (scale bar, 1 mm). Insets show enlarged images of the SNr and Pf. Similar results were obtained in  $n=2$  mice. **c**, Protocol as in **a** but with Cre- and Flpo-dependent viruses injected in SNr to label the medial and lateral SNr target zones (<sup>M</sup>SNr and <sup>L</sup>SNr). **d**, Example coronal sections showing the infected cell bodies in SNr (left) and their axons downstream of the SNr (right three panels) in VM, Pf and SC (scale bar, 1 mm). Insets show enlarged images of the VM and Pf. Similar results were obtained in  $n=4$  mice. **e**, Protocol for anterograde tracing from more localized, focal injections of AAV1-Cre into DMS, DLS or VLS in separate mice, followed by an AAV-DIO-TdTom in SNr. **f**, Example coronal sections showing the infected cell bodies in SNr (left column) and axons in Pf, VM, SC and BS (right four columns) for mice with AAV1-Cre injections into DMS, DLS or VLS, as indicated. Scale bar, 250  $\mu$ m. Similar results were obtained in  $n=9$  mice ( $n=3$  for each site).

Flpo-dependent manner in downstream targets (GPe and SNr) (Fig. 2a,c). This allowed simultaneous examination of the target regions of the two striatal injection sites in each output structure as well as the distribution of the axons from the output structure subregions to their downstream targets. We used this strategy to examine the projections of medial and lateral striatum through the GPe and SNr to downstream regions. We injected a larger volume of AAV1-Cre than in the previous experiment (Fig. 1b) to label as many cells as possible in the downstream areas. This approach revealed BG pathways through GPe arising from inputs in medial or lateral striatum (<sup>M</sup>GPe or <sup>L</sup>GPe, respectively) (Fig. 2b). <sup>M</sup>GPe and <sup>L</sup>GPe axons targeted SNr, Pf, striatum and cortex, consistent with previous studies (Fig. 2b)<sup>17,32</sup>. Furthermore, in these targets, topographical organization was observed whereby <sup>M</sup>GPe innervated medial SNr, medial striatum, medial Pf and limbic cortical regions, whereas <sup>L</sup>GPe innervated lateral SNr, lateral striatum, ventrolateral Pf and sensorimotor cortical regions (Fig. 2b). A similar approach was used to investigate the topography downstream of SNr and EP

(Fig. 2c and Extended Data Fig. 2). A medial-lateral topographical arrangement was observed downstream of SNr, in VM, Pf, SC and zona incerta, as well as downstream of EP, in lateral habenula (Fig. 2d and Extended Data Figs. 2–5).

Given the fine-scale topographical organization observed from DMS, DLS or VLS to SNr (Fig. 1d), we hypothesized that a similar fine-scale topography might also exist downstream of SNr, with higher precision than that we observed for medial versus lateral SNr projections (Fig. 2d). Labeling three pathways simultaneously in one mouse was challenging, due to a lack of a third recombinase that could work along with Cre and Flpo. Therefore, we focally injected AAV1-Cre in DMS, DLS or VLS in H2B reporter mice (as in the experiment described in Fig. 1), followed by AAV-DIO-TdTom into SNr. Crucially, we ensured that focal AAV1-Cre injections in the striatum did not invade neighboring regions. As expected, TdTom-positive cells were observed in different parts of SNr, depending on the location of the AAV1-Cre injection in striatum. We quantified relative axonal density in the brain regions downstream

of SNr for the three striatal injection sites (DMS, DLS and VLS; Fig. 2e,f and Extended Data Fig. 6). All SNr subregions targeted brain regions in a similar fashion, with heaviest innervation in ventromedial/ventral anterior thalamus (VM/VA), SC and zona incerta. Axons in Pf, VM, SC and brain stem (intermediate reticular nucleus (IRt)/parvicellular reticular nucleus (PCrT) and gigantocellular reticular nucleus (Gi)) were topographically organized, similar to what was observed above (Fig. 2c,d) but at a finer scale (Fig. 2f). Interestingly, in SC, DMS recipient SNr ( $^{DMS}SNr$ ) axons and DLS recipient SNr ( $^{DLS}SNr$ ) axons both innervated the medial part of SC, but close inspection revealed differential layer specificity (Extended Data Fig. 4), in a manner that segregated projections within medial SC, and similar to previous observations<sup>33</sup>. We also observed axons within striatum, representing putative dopamine neurons labeled via anterograde tracing. Axons within striatum overlapped with the striatal injection site, suggesting closed loops between striatum and midbrain dopaminergic centers (Extended Data Fig. 7a). In separate experiments, we confirmed that axons observed in striatum did not arise from non-dopaminergic SNr cells (Extended Data Fig. 7b–d). Overall, BG pathways starting from DMS, DLS and VLS maintained anatomical segregation outside of the BG.

**SNr output forms closed and segregated loops via VM, Pf and SC.** The thalamic nucleus Pf is one of the main glutamatergic input structures to striatum and its projection to striatum is topographically organized<sup>34</sup>. As the SNr output to Pf is also topographically organized, point-to-point closed BG loops through thalamus may exist. To verify the existence of closed and segregated BG loops via Pf, we re-examined sections containing Pf from experiments described above (Fig. 2e,f). We noticed that AAV1-Cre acted as both an anterograde and a retrograde tracer, consistent with the previous report<sup>27</sup>. This permitted examination of retrogradely labeled Pf cells that project to DMS, DLS or VLS, and anterogradely labeled SNr axons ( $^{DMS}SNr$ ,  $^{DLS}SNr$  and  $^{VLS}SNr$ ) in Pf simultaneously (Fig. 3a). Consistent with the existence of closed and segregated loops, anterogradely selected SNr axons and retrogradely labeled Pf cells colocalized within Pf for all injections into DMS, DLS and VLS (Fig. 3b).

To examine whether these SNr→Pf projections made synaptically connected but segregated networks, as suggested by the anatomy, we used whole-cell electrophysiology to examine synaptic transmission in acute brain slices from mice in which we performed both anterograde and retrograde tracing. We first injected red fluorophore-tagged Cholera Toxin subunit B (CTB, retrograde tracer) into DMS, green fluorophore-tagged CTB into DLS and AAV1-Cre into one of these two regions, followed by AAV-DIO-CoChR<sup>35</sup>, an efficient variant of ChR2, in SNr (Fig. 3c). Using this approach, we obtained acute brain slices of Pf with DMS-projecting and DLS-projecting Pf neurons ( $Pf_{DMS}$  and  $Pf_{DLS}$ ) marked by red and green CTB, and with CoChR expressed in either  $^{DMS}SNr$  or  $^{DLS}SNr$  axons. Examining slices from mice in which AAV1-Cre was injected in DMS to express CoChR in  $^{DMS}SNr$ , we found stronger and more-probable GABAergic connections for  $^{DMS}SNr$ → $Pf_{DMS}$  than for  $^{DMS}SNr$ → $Pf_{DLS}$  projections (Fig. 3d,  $P < 10^{-3}$ ). Examining slices from mice in which AAV1-Cre was injected in DLS, we found the opposite pattern, with  $^{DLS}SNr$ → $Pf_{DLS}$  making stronger inhibitory connections compared with  $^{DLS}SNr$ → $Pf_{DMS}$  (Fig. 3d,  $P < 10^{-4}$ ). Together, these results indicate that anatomically segregated BG loops via Pf are functionally closed and synaptically segregated.

VM projects heavily to layer 1 in nearly all of the cerebral cortex<sup>36,37</sup>. We also observed that SNr recipient VM projected throughout large parts of the cortex, and most heavily to layer 1 (Fig. 4a,b). To test whether individual cells within VM specifically target certain cortical regions, we injected three different-colored retrograde tracers (CTBs) into layer 1 of the anterior cingulate

cortex (ACA), forelimb motor cortex (fM1), and tongue and jaw motor cortex (tjM1) in the same mouse. These frontal regions project to DMS, DLS and VLS, respectively<sup>29,30</sup>. Retrograde CTB tracing via layer 1 in the cortex revealed a fine topography in VM-to-cortex layer 1 projections (Fig. 4c). Interestingly, the topographical organization revealed by CTB injections closely matched that of SNr axons (Fig. 2f), suggesting the existence of segregated thalamocortical BG loops via VM.

To functionally confirm the existence of such thalamocortical BG loops, as well as to test the degree of segregation between different SNr→VM pathways, we conducted similar acute slice physiology experiments as in Fig. 3. Given that thalamocortical BG loops involve one extra synapse compared with thalamostriatal BG loops, we could not trace the entire loop in a single experiment using available tools. Thus, we exploited the fact that topography was maintained in cortex (CTX)→striatum (STR) and used CTB to retrogradely label VM neurons based on their cortical output. We examined the segregation of  $^{DMS}SNr$ → $VM_{ACA}$  and  $^{DLS}SNr$ → $VM_{fM1}$ , two neighboring SNr output pathways, by combining anterograde tracing, AAV-DIO-CoChR transduction in SNr and retrograde labeling of VM neurons (Fig. 4e).  $VM_{ACA}$  and  $VM_{fM1}$  projection neurons were retrogradely labeled via CTB injections into corresponding cortical regions. AAV1-Cre was subsequently injected into striatum, targeting either DMS or DLS, followed by AAV-DIO-CoChR injection into SNr. Brain slices containing both  $VM_{ACA}$  and  $VM_{fM1}$  neurons, along with either CoChR-expressing  $^{DMS}SNr$  or  $^{DLS}SNr$  axons, were used to examine functional synapses formed onto both VM populations. Consistent with segregated SNr topography to VM, we found strong GABAergic connections for  $^{DMS}SNr$ → $VM_{ACA}$  and for  $^{DLS}SNr$ → $VM_{fM1}$ , but not vice versa (that is, across pathways) (Fig. 4f). These results indicate the existence of functionally segregated thalamocortical BG loops via VM.

Although SC has been traditionally described as a target region of BG that projects to the brain stem, SC also projects back to thalamus, potentially forming recurrent subcortical loops<sup>38–40</sup>. We examined whether SC also forms topographically organized subcortical loops. Labeling SC cells based on the topographical output of SNr neurons was challenging due to the difficulty of targeting distinct populations within the small SNr. However, we noticed that certain cortical regions (ACA cortex, fM1 and tjM1) innervate SC in a topographical fashion, almost exactly mirroring the topography of SNr axons<sup>41</sup> (Extended Data Fig. 8a). Therefore, we used cortex to anterogradely label distinct SC cells, which might potentially be downstream of  $^{DMS}SNr$  and  $^{VLS}SNr$  axons, by injecting an AAV1-Cre and AAV1-Flpo into ACA and tjM1, respectively. We injected AAV1-DIO-TdTom and AAV1-fDIO-EYFP into SC, thus labeling each SC cell population with a different fluorophore. We observed that SC cells downstream of ACA ( $^{ACA}SC$ ) and tjM1 ( $^{tjM1}SC$ ) were located in medial and lateral SC, respectively (Extended Data Fig. 8c). Furthermore, these cells innervated distinct regions of Pf and VM (Extended Data Fig. 8d). Comparing results from Figs. 3b and 4d with the SC topography confirmed the existence of BG loops via SC, whereby  $^{ACA}SC$  (or putative  $^{DMS-SNr}SC$ , that is, SC cells downstream of  $^{DMS}SNr$ ) and  $^{tjM1}SC$  (putative  $^{VLS-SNr}SC$ ) project to  $Pf_{DMS}/VM_{ACA}$  and  $Pf_{VLS}/VM_{fM1}$ , respectively.

**Focal activation of striatum reveals functional maps for licking/orienting.** The *trans*-synaptic tracing indicated that SNr neurons that receive input from distinct striatal regions innervate distinct parts of VM, Pf, SC and brain stem. Specifically, we found that  $^{VLS}SNr$  projects to orofacial brain regions, including lateral SC, PCrT and IRt<sup>23,42</sup>, whereas  $^{DMS}SNr$  axons innervate medial SC and Gi, regions that have been implicated in escape, avoidance and locomotor behaviors<sup>26,43,44</sup> (Fig. 2f and Extended Data Fig. 6b). Hence, we reasoned that distinct striatal regions (DMS and VLS) might modulate distinct behaviors, with, specifically, VLS controlling

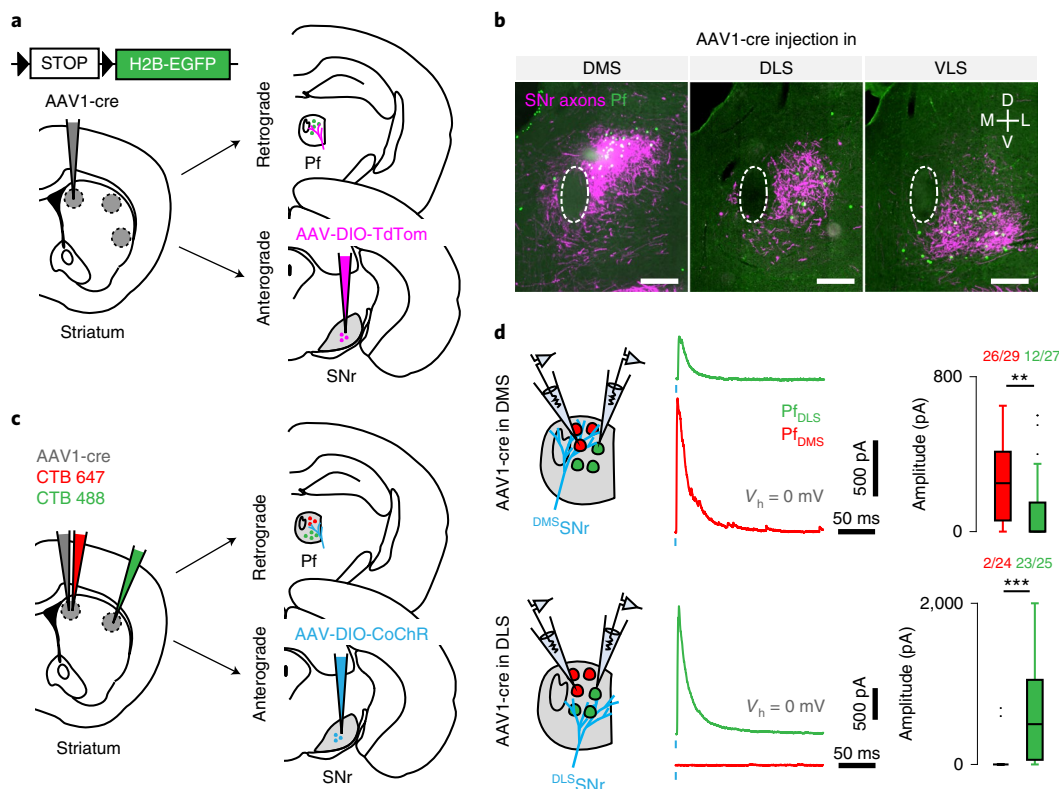


**Fig. 3 | The BG output via Pf forms segregated and closed loops.** **a**, Simultaneous mapping of Pf input to striatum and BG output to Pf. AAV1-Cre injected into the H2B-EGFP reporter mouse travels retrogradely to label neurons in Pf that project to the injection site as well as anterogradely to labels neurons in SNr targeted by those in the injection site. AAV-DIO-TdTom injected into SNr labels axons in Pf arising from SNr neurons that are in the zone targeted by neurons in the striatal injection site. **b**, Overlap of retrogradely labeled Pf cells (green) and axons (magenta) from anterogradely labeled SNr cells for different locations of striatal injection (column, DMS, DLS or VLS). Scale bar, 250  $\mu\text{m}$ . Similar results were obtained in  $n = 9$  mice ( $n = 3$  for each site). **c**, Testing topography in slices. Pf cells were retrogradely labeled via CTB injection from two striatal locations, while only one striatal location also received an AAV1.Cre injection. The entire SNr was injected with AAV-DIO-CoChR. Connection strength was tested by patching in voltage clamp and comparing outward current in either DMS-projecting cells (red) or DLS-projecting cells (green) inside Pf. **d**, Left: example outward currents observed in distinct Pf cells (red,  $\text{Pf}_{\text{DMS}}$ ; green,  $\text{Pf}_{\text{DLS}}$ ) after optogenetic stimulation of SNr axons (blue line). Each row indicates experimental conditions where the location of AAV1.Cre injection was varied (top, DMS; bottom, DLS). Right: box plot quantification of peak amplitude of outward currents and number of connected cells of all cells tested (top, 56 cells from 3 mice; bottom, 49 cells from 3 mice) (\*\* $P < 10^{-3}$ , \*\*\* $P < 10^{-4}$ , one-sided Mann-Whitney  $U$ -test). Box depicts 25th percentile, median and 75th percentile, and whiskers depict  $\pm 2.7$  s.d.; data points outside these ranges are shown as individual circles.

coordinated orofacial movements such as licking and DMS controlling body movements such as orientation during locomotion.

To test this hypothesis, we first developed a tapered fiber (TF) laser launch and control system<sup>45,46</sup> that delivers light via a tapered optical fiber at distinct and rapidly selectable depths along the tapered tip of the TF (Fig. 5a and Extended Data Fig. 9). We used a higher-numerical aperture (NA) TF (0.66 NA) than the 0.39 NA used previously<sup>47</sup> to improve the resolution of stimulation and to increase the number of sites that could be stimulated per fiber. We confirmed the ability to scan light output from the TF (0.66 NA, diameter 200  $\mu\text{m}$ , emitting length = 2,500  $\mu\text{m}$ ) to achieve local excitation by placing it in a fluorescein solution and stepping the laser input between four different angles. Peaks of the intensity profile were well separated for four distinct angles corresponding to four distinct depths along the TF (Fig. 5b).

We validated the use of a TF for activating focal regions in vivo by simultaneously stimulating and recording extracellular activity within striatum using a ‘fibertrode’ consisting of a TF attached in parallel (spacing  $\sim 300 \mu\text{m}$ ) to a silicon multielectrode array (Fig. 5c–e). We examined activation of CoChR-expressing indirect pathway striatal projection neurons using AAV-DIO-CoChR injected into an *Adora2a-Cre* transgenic mouse because these neu-

rons form only local inhibitory synapses and do not excite striatum via recurrent feedback projections, permitting unambiguous identification of optogenetically activated neurons. Distinct units were activated along the dorsoventral axis when stimulating at different depths using low-intensity laser pulses (1,000 ms, 100  $\mu\text{W}$ ), over a depth range of 2,400  $\mu\text{m}$  (Fig. 5d,e). Thus, TFs allow focal activation of distinct populations of neurons along the dorsoventral striatal axis.

To reveal which region in striatum is capable of modulating licking, we designed a lateralized licking task in which mice had to lick either to the left or to the right spout, depending on the frequency of a tone, to collect a water reward (Fig. 6). A low-frequency tone indicated that the mouse should lick to the left and a higher-frequency tone indicated that the mouse should lick to the right. The first lick after the tone onset was considered the choice lick and, if it was made to the ‘correct’ direction, a water reward was delivered. After  $\sim 2$  weeks of training, mice became expert at the task, achieving high performance accuracy ( $88.2 \pm 2.2\%$  correct trials, mean  $\pm$  s.e.m.,  $n = 5$  mice). Mice licked on average an additional seven times to collect reward on the correct trials and three times on the incorrect trials, despite absence of a reward. The latency from tone onset to the choice lick was  $195 \pm 23$  ms and the interlick interval was

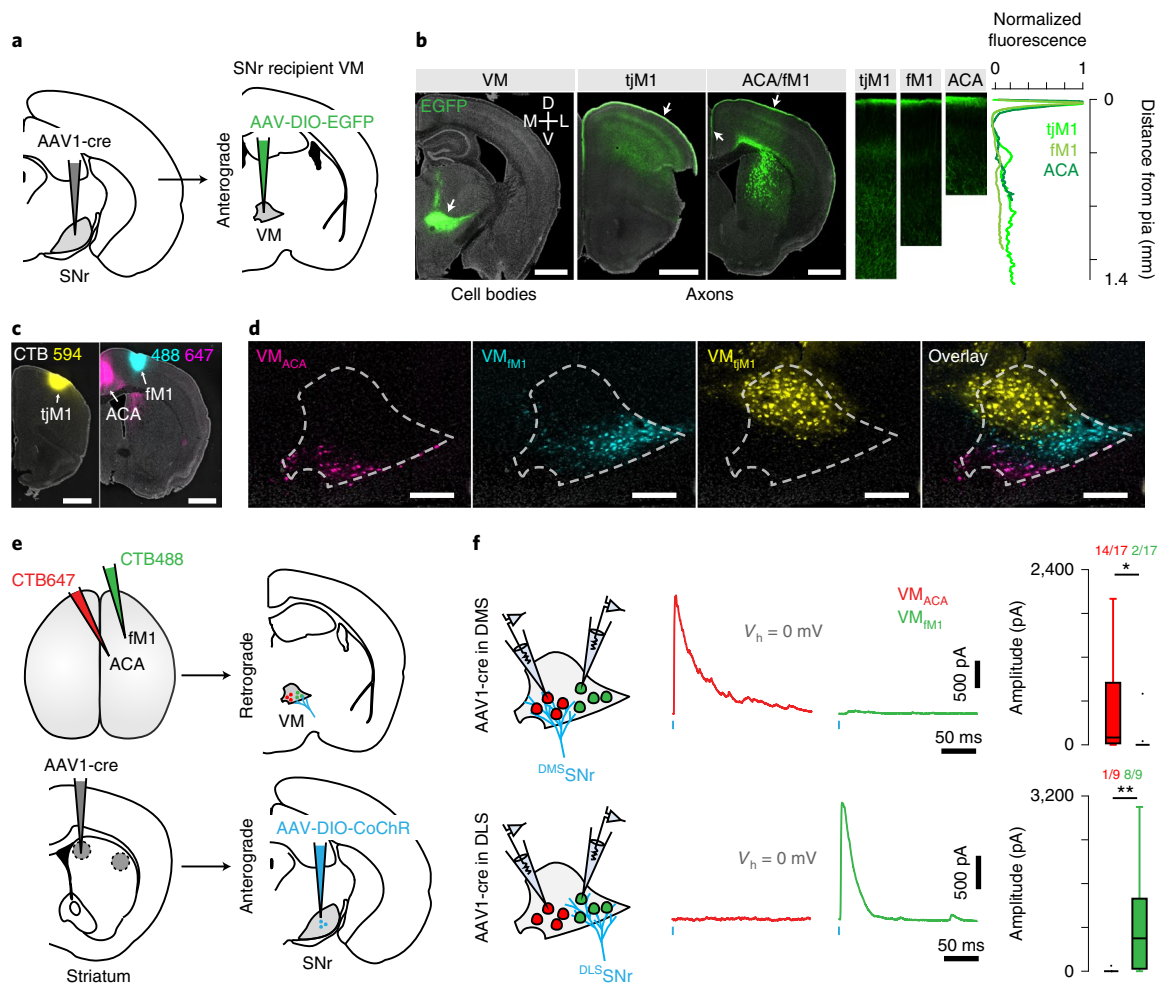


**Fig. 4 | BG output via VM forms segregated closed loops via cortical layer 1.** **a**, Protocol for labeling SNr recipient VM neurons. AAV1-Cre was injected in SNr followed by AAV-DIO-EGFP in VM. **b**, Left: coronal section showing injection site and labeled cell bodies in VM. Center: labeled VM axons target many layers and densely innervate layer 1 throughout frontal cortex (shown here are tjM1, ACA and fM1 in white arrows). Right: quantification of EGFP fluorescence intensity across cortical depth in the indicated cortical regions. Similar results were obtained in  $n = 3$  mice. Scale bar, 1 mm. **c**, Coronal section showing the injection sites of three different-colored retrograde tracers (CTB594, CTB488 and CTB647 shown in yellow, cyan and magenta, respectively) in superficial layers of tjM1, fM1 and ACA. Scale bar, 1 mm. **d**, Coronal sections showing retrogradely labeled VM cells (tjM1, yellow; fM1, cyan; ACA, magenta). Similar results were obtained in  $n = 3$  mice. Scale bar, 250  $\mu\text{m}$ . **e**, Protocol for examining the segregation of DMS and DLS SNr output pathways in VM. Two different-colored CTBs were injected into layer 1 of either ACA or fM1, AAV1-Cre was injected focally in the striatum (either DMS or DLS) and AAV-DIO-CoChR was injected broadly in the SNr. **f**, Left: schematic of the acute preparation for whole-cell physiology. Whole-cell voltage-clamp recordings were obtained from VM cells retrogradely labeled from ACA (red) or fM1 (green), and optogenetically evoked outward currents were measured at a holding potential ( $V_h$ ) of 0 mV. Center: example outward currents in VM<sub>ACA</sub> or VM<sub>fM1</sub> after optogenetic stimulation of SNr axons (blue line). Right: box plot quantification of average peak amplitude of outward currents evoked across all cells. In all columns, the top and bottom rows show results from experiments in which AAV-Cre was injected into DMS and DLS, respectively (top,  $n = 34$  cells, 3 mice; bottom,  $n = 18$  cells, 2 mice) (\* $P < 10^{-2}$ , \*\* $P < 10^{-3}$ , one-sided Mann-Whitney  $U$ -test). Box depicts 25th percentile, median and 75th percentile, and whiskers depict  $\pm 2.7$  s.d.; data points outside these ranges are shown as individual circles.

$133 \pm 5$  ms, consistent with reported lick frequency during water consumption<sup>23</sup>.

To reveal the functional organization of striatum in controlling licking behavior, we examined the effect of optogenetically activating the direct pathway striatal projection neurons (dSPNs) during different task phases in well-trained mice. *Drd1a-Cre* mice, which express Cre recombinase in dSPNs<sup>48</sup>, were injected with AAV-DIO-CoChR and implanted with two TFs covering DMS, DLS and VLS (Fig. 6a,b) to achieve multi-site striatal activation. Each fiber was used to target four distinct depths; we used the medial fiber top site to target DMS, lateral fiber bottom site to target VLS and lateral fiber top site to target DLS (see Methods). Fully trained mice were stimulated at different locations along the medial or lateral fibers at

randomly interleaved trials during the inter-trial interval (Fig. 6c,d and see Methods). Importantly, fully trained mice rarely licked during this period (Fig. 6f), allowing unambiguous testing of the effect of stimulating dSPNs. Brief stimulation (100 ms, 100  $\mu\text{W}$ ) of dSPNs during the inter-trial interval caused mice to lick to the contralateral spout (Fig. 6e-g), with the magnitude of effects depending on the site of stimulation. Probability of licking to the contralateral spout was strongest for stimulation in the VLS ( $94.1 \pm 2.1\%$ ) and weaker in DLS ( $27.8 \pm 7.9\%$ ) and DMS ( $1.6 \pm 0.9\%$ ), consistent with the VLS SNr projections controlling lick-related brain regions. Median lick latency after stimulating VLS was 192 ms (from laser onset), which was slower but comparable to the tone-induced lick latency (98 ms). Successful VLS stimulation also generated a median of 3

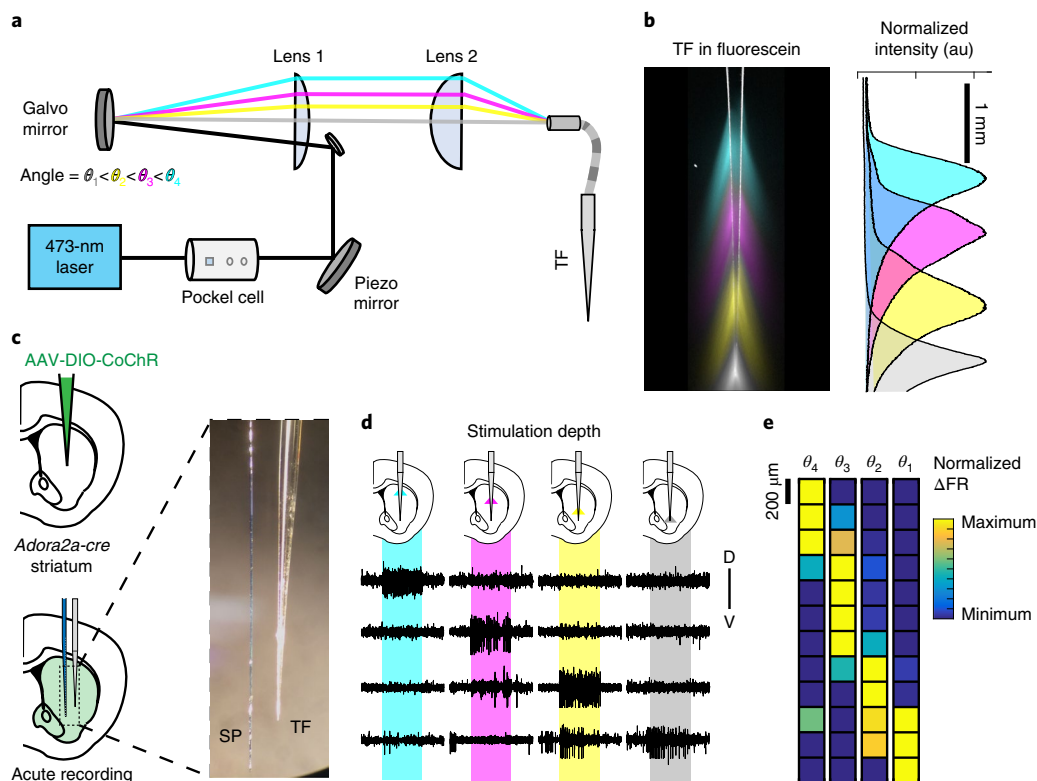


**Fig. 5 | Focal optogenetic stimulation of neurons in striatum using TF optics.** **a**, Optical setup for depth-dependent stimulation via TFs (see Methods). A steering galvanometer mirror controlled the angle at which a laser beam entered the patchcord (colors indicate four possible incident angles of the laser beam). **b**, Left: color-coded fluorescence profiles generated by a TF inside fluorescein solution with light entering the patchcord at four different angles. Right: quantification of the normalized fluorescence intensity profile along the axis of the fiber. Scale bar, 1 mm. **c**, Experimental preparation for in vivo validation of focal optogenetic stimulation of striatal neurons. CoChR was expressed selectively in indirect pathway striatal projection neurons by injection of AAV-DIO-CoChR into the striatum of an *Adora2a-Cre* transgenic mouse. After expression of the optogenetic protein, a fiberprobe consisting of a TF attached parallel to a silicon probe (SP) was acutely implanted into the striatum of a head-restrained animal. **d**, Example session with multi-units at different depths along the electrode recorded while light was emitted from different depths along the TF. Each row shows raw channel traces from contacts at different depths (dorsal to ventral, top to bottom). The colored bars indicate the time of laser illumination at each input angle and the corresponding emission at each depth. **e**, Quantification of normalized change in firing rate for units at different depths of stimulation (column). Each square represents multiple units pooled from two channel sites spanning 200  $\mu\text{m}$  (see Methods). au, arbitrary units;  $\Delta\text{FR}$ , change in firing rate relative to baseline;  $\theta$ , galvo mirror angle.

licks (range, ~1–13 licks), despite the stimulation being shorter than the average inter-lick interval. This indicates that coordinated jaw opening, tongue protrusion and multiple lick cycles can be induced by a brief stimulation of dSPNs in the VLS.

To test whether dSPN stimulation in specific striatal subregions also influences the animal's lick direction during a motivated and cued action for reward, we stimulated the same mice during tone presentation. Stimulation in VLS starting 25 ms after the tone onset, and lasting for 100 ms, biased the mouse to lick to the left on right-cued trials, but had no effect on left-cued trials (Fig. 7a). Stimulation applied to DMS did not influence lick direction on either left- or right-cue trials (Fig. 7b). Overall, the striatal region that influenced the mouse decision during tone stimulation matched the region effective at driving licking with inter-trial interval (ITI) stimulation (Fig. 7c,d), indicating that dSPN activation can override the cue-driven licking decision, whereas similar activation in regions outside of this lick zone does not interfere with licking behavior. Thus, dSPN activation in a specific striatal subregion can both trigger a motor action and influence ongoing decisions. Furthermore, activation of dSPNs in regions outside of the VLS lick zone does not interfere with licking, supporting the parallel model of BG function.

Given that BG outputs target many brain regions (Fig. 2e,f), dSPN activation of a striatal region associated with a motor action

may induce activity in both cortical and subcortical components of the anatomically defined loop. To examine this possibility, we performed extracellular recording in tJM1 and lateral SC, two regions downstream of <sup>VLS</sup>SNr, while mice performed the licking task, and activated VLS dSPNs (Extended Data Fig. 10a). Given that <sup>VLS</sup>SNr projects directly to lateral SC and indirectly to tJM1 via VM (Figs. 2e and 4), we reasoned that activation of striatum should modulate activity in these regions if the BG loops were functionally engaged in vivo. As predicted, activation of VLS dSPNs increased the activity of most of the units recorded in both tJM1 and lateral SC (Extended Data Fig. 10b–d). This effect occurred during both ITI and tone presentation, but was weaker on left compared to right trials, consistent with the presence of behavioral effects only on right trials (Fig. 7). Overall, this indicates that dSPN activity in a striatal subregion that is effective at driving an overt behavior engages multiple regions within the BG loop associated with the same behavior.

Based on our anatomical analysis of <sup>DMS</sup>SNr projection targets, and the reported functions of these regions, we reasoned that the DMS might be involved in turning or locomotor behavior. Therefore, we placed the mice that had been trained on the licking task in an open field and stimulated the same eight regions while the mice freely explored a square arena (Fig. 8a). Stimulation led to

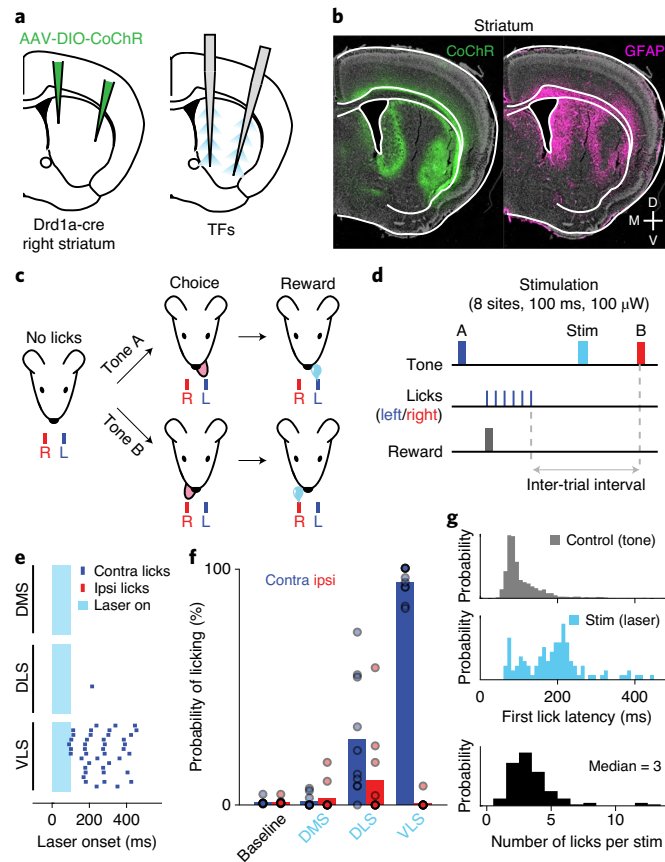


**Fig. 6 | Stimulation of direct pathway projection neurons in VLS induces contralateral licking.** **a**, Experimental protocol to achieve focal optogenetic stimulation of direct pathway neurons in striatum. AAV-DIO-CoChR was injected into the right striatum in *Drd1a-Cre* mice and two TFs were implanted in the medial and lateral parts of the striatum. **b**, Example coronal section of a *Drd1a-Cre* mouse processed after training. Left: CoChR expression (green); right: GFAP immunostaining (magenta) show the location of the fibers in the striatum. **c**, Task structure. Mice were trained to lick either a left or a right water reward port after hearing tone A or B, respectively (see Methods). The first lick was considered the choice lick and, if directed towards the correct port, triggered delivery of a water drop reward at the corresponding spout. Mice had to refrain from licking during the random intertrial interval (2–4 s) for the next tone to be played. **d**, Stimulation protocol showing that one of eight sites (four lateral and four medial) was stimulated optogenetically (100 ms, 100  $\mu$ W) during the inter-trial interval. **e**, Example session showing lick raster aligned to laser onset for stimuli delivered to different striatal locations (DMS, DLS and VLS). **f**, Probability of contralateral (blue) or ipsilateral (red) water port licking within 500 ms of laser onset for stimulation of DMS, DLS and VLS. Data are shown as mean  $\pm$  s.e.m. across ten sessions from  $n=5$  mice. **g**, Latency and number of stimulation-induced licks. Top: the distribution of first lick latency relative to tone onset (5 mice, 10 sessions, 2,123 trials). Middle and bottom: distributions of first lick latency and the number of licks for all lick-induced optogenetic stimuli (119 trials, 5 mice, 10 sessions), respectively. L, left; R, right.

robust turning contraversive to the stimulation side in a site-specific manner (Fig. 8b). The effect was strongest for stimulation of VMS and DMS, and weaker for VLS and DLS (Fig. 8c,d), indicating that regions most effective at inducing licking were relatively ineffective at inducing turning. For all striatal regions stimulated, we quantified the magnitude of turning and probability of licking induced by stimulation in the licking task described above (Fig. 8e,f). Turning was most effectively induced in the medial sector of striatum, with the strongest effect coming from a slightly ventral region (VMS), whereas licking was most effectively induced in the ventrolateral striatal region (VLS). Thus, the anatomically and synaptically segregated pathways described above that target distinct thalamic, collicular and brain stem regions generate different motor outputs.

## Discussion

Here, we anatomically and functionally dissected outputs of the mouse BG using an anterograde tracer and a method to focally activate distinct striatal regions in individual mice<sup>27,28,46,47</sup>. We provide

direct anatomical evidence for the existence of at least three closed loops starting from DMS, DLS and VLS and passing through Pf, VM or SC. Functionally, we show that the DMS and VLS pathways modulate contraversive turning and licking, respectively. Crucially, regions outside of the VLS did not modulate ongoing lick decisions, suggesting parallel organization of BG output. VLS dSPN activation engaged BG cortical and collicular loops, suggesting that the BG loops are functionally active in vivo. Our results likely generalize to other striatal regions involved in other behaviors, and provide a framework to investigate functionally and anatomically isolated BG circuits.

**Anterograde labeling as a tool to study small BG nuclei.** Cascading circuits within the BG are organized with increasing anatomical convergence such that each downstream nucleus is smaller and has fewer neurons than its upstream partners. This convergent nature of BG circuits poses a challenge for focal tracing and manipulations of small BG output nuclei by virus injection. We take advantage of AAV1, which, as previously demonstrated, allows the anterograde



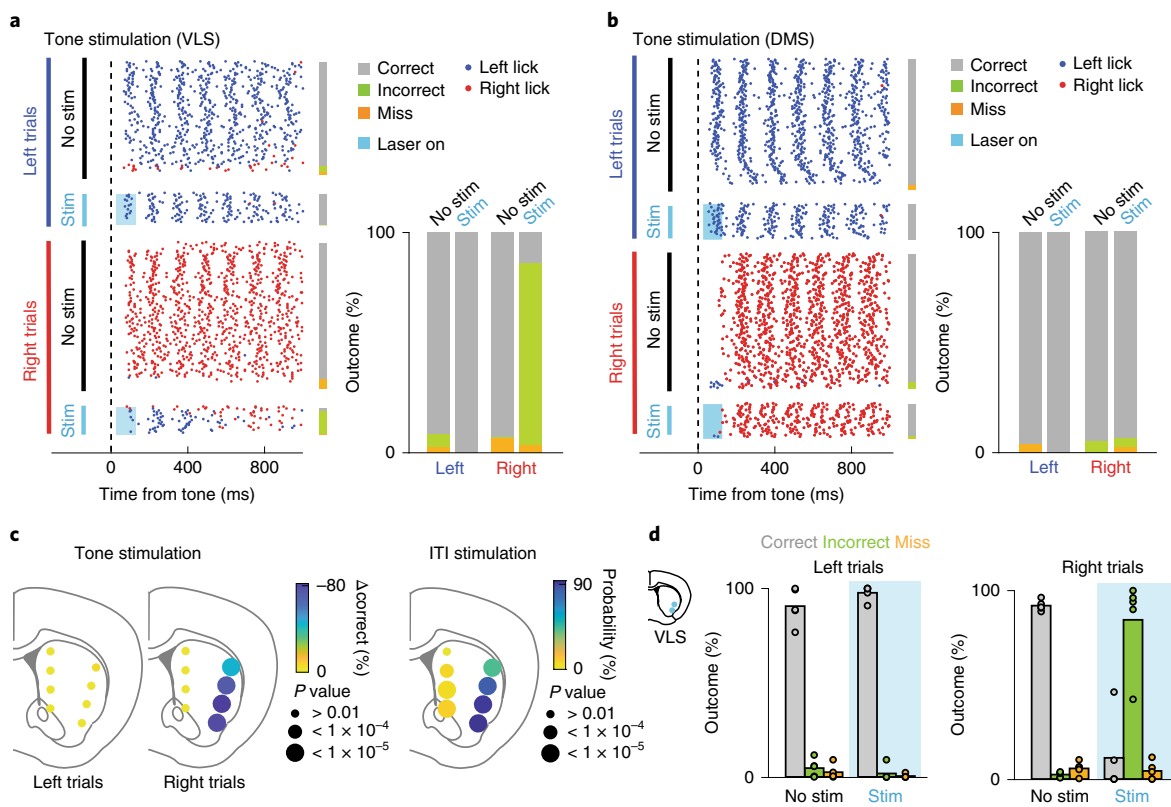


**Fig. 7 | dSPN stimulation outside of VLS does not interfere with cue-evoked licking.** **a**, Left: example session where dSPN stimulation was applied in VLS during tone presentation (see Methods). Each dot represents a spout contact on the left (blue) or right (red) relative tone onset. Trials are sequentially sorted by trial type (left versus right), stimulation (no stim versus stim) and outcome (correct versus incorrect versus miss). Right: summary of the outcomes for left trials and right trials for the example session shown on the left. Stimulation on right trials, but not left trials, caused a significant increase in incorrect outcome percentage. **b**, Left: example session in which dSPN stimulation was applied to DMS. Right: stimulation did not change the percentage outcome for both left and right trials. **c**, Left: summary graph for eight striatal sites stimulated for left and right trials during tone presentation. Each circle represents a single striatal site of stimulation, with the color representing the change in percentage of correct outcomes (%) and the size representing the  $P$  values. Only stimulation on the right trials in VLS decreased the performance. Right: summary graph for ITI stimulation (Fig. 6).  $P$  values were calculated by bootstrapping (see Methods). (Tone stimulation left trials, DMS/VMS fiber:  $P=0.90, 0.95, 0.86, 0.25$ ; DLS/VLS fiber:  $P=0.99, 0.77, 0.56, 0.026$ . Tone stimulation right trials, DMS/VMS fiber:  $P=0.65, 0.93, 0.62, 0.71$ ; DLS/VLS fiber:  $P=10^{-5}$  for all sites. ITI stimulation, DMS/VMS fiber:  $P=10^{-5}, 10^{-5}, 2.0 \times 10^{-5}, 1.5 \times 10^{-2}$ ; DLS/VLS fiber:  $P=10^{-5}$  for all sites. All  $P$  values from each fiber reported from bottom to top site.) **d**, Breakdown of change in outcome (%) for VLS stimulation in left and right trials. Summary graph for left and right trials for no-stim and stim trials. Each dot represents a session from one individual mouse ( $n=5$  mice). Each trial outcome is categorized into correct (gray), incorrect (green) or miss (orange). Stimulation on the right trials increased the percentage incorrect (%) relative to no-stim trials.

movement of a small amount of virus to activate transgene expression in downstream areas<sup>27,28</sup>. Specifically, we show that it is possible to *trans*-synaptically deliver Cre in small subregions of GPe, EP or SNr that receive input from DMS, DLS or VLS. The simultaneous use of AAV1s encoding different recombinases permits comparisons of multiple anatomical features in the same mouse. Although we restricted our analysis to these three striatal regions, one could apply the same strategy to any striatal region of interest. This allows a targeted approach to study the anatomy of specific subregions of those nuclei and to test their necessity and sufficiency in behaviors of interest.

**Unifying principles of BG output organization.** Using focal injection of the anterograde tracer, we were able to study the output organization of SNr in great detail. Our results suggest two main principles of BG output organization. First, all BG pathways surveyed innervated VM, Pf and SC, albeit in a topographically organized manner. Thus, unique projection motifs (that is, a pure VM-projecting pathway or a pure SC-projecting pathway) do not exist within each pathway, and thus cannot explain the functional

differences between these pathways observed after stimulation. Second, all regions targeted by SNr (at least VM, Pf and SC) project back to the striatal region from which the SNr input arises, thus forming closed recurrent loops. Although we restricted our analysis to VM, Pf and SC, it is possible that similar topographical loops exist for other SNr targets<sup>9</sup>.

**Functional segregation within striatum.** Our functional analyses were enabled by the use of TF optics to deliver and dynamically move focal stimulation that is effective at low light powers<sup>47</sup>. Using this approach, we found that DMS and VMS stimulation causes contralateral turning whereas focal stimulation of VLS causes contralateral licking. This is in agreement with their respective anatomical projections via SNr to downstream regions, suggesting that the function of striatal subregions can be predicted by their SNr projection targets. VLS stimulation also engaged tjM1 and lateral SC, regions that are downstream of VLS-SNr, suggesting that the BG circuits described earlier are functionally engaged *in vivo*.

Previous studies have shown that optogenetic stimulation of the DLS direct pathway can cause contralateral turning as well as

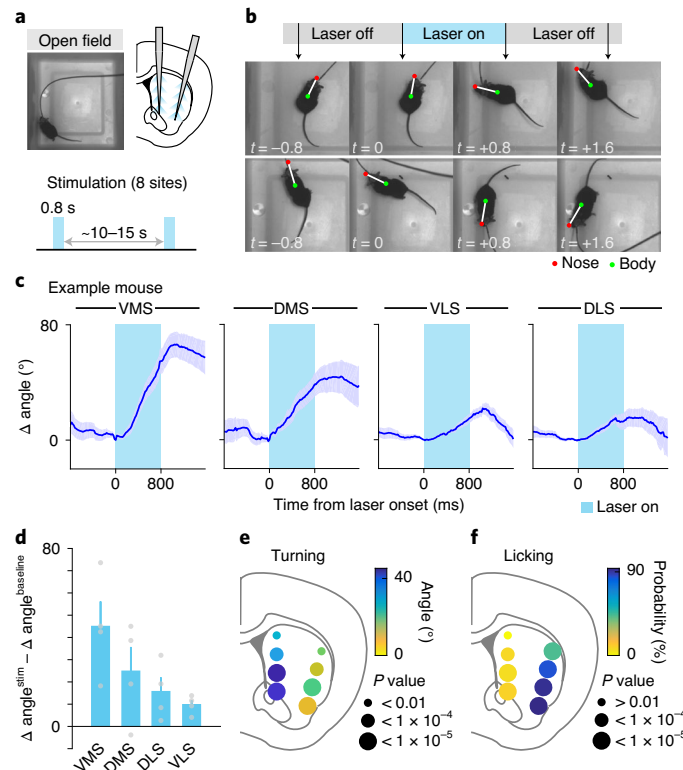


**Fig. 8 | DMS and VMS direct pathway stimulation induce contralateral turning.** **a**, Experimental protocol for examining the effects of focal striatal stimulation on turning. A mouse was placed in an open field arena and optogenetic stimuli were delivered to different striatal regions via TFs for 0.8 s every -10–15 s (see Methods). **b**, Two example trials in which stimulation in medial striatum induced contralateral turning. Time relative to laser onset is indicated in white at the bottom left for each frame. The nose and body positions are indicated in red and green, respectively. **c**, Example session for one mouse showing cumulative turn angle relative to laser onset (defined as 0 degrees) for stimulation in VMS, DMS, VLS and DLS (left to right). The period during which the laser was on is indicated in blue (20 trials per stimulation site). Data are shown as mean  $\pm$  s.e.m. across trials. **d**, Baseline-subtracted turn angle (cumulative angle turned during stimulation – cumulative angle turned before stimulation; see Methods) for VMS, DMS, VLS and DLS. Data are shown as mean  $\pm$  s.e.m. across mice ( $n=4$ ). VMS was defined as the second site from the bottom in the DMS/VMS fiber. **e**, Contralateral turn angle for all eight stimulated regions. The color of each circle indicates the effect size (baseline-subtracted cumulative turned angle in degrees), whereas its size indicates the  $P$  value (DMS/VMS fiber:  $P=10^{-5}$ ,  $10^{-5}$ ,  $2.3 \times 10^{-4}$ ,  $2.4 \times 10^{-3}$ ; DLS/VLS fiber:  $P=10^{-5}$ ,  $10^{-5}$ ,  $3.5 \times 10^{-4}$ ,  $7.3 \times 10^{-3}$ . All  $P$  values from each fiber reported from bottom to top site). **f**, As in **e** but showing contralateral lick probability in lateralized licking task for stimulation during ITI (right panel from Fig. 7c, reproduced for comparison).  $P$  values were calculated by bootstrapping (Fig. 7c).

licking<sup>20,49</sup>. Interestingly, the focal and low-power-intensity stimulation approach used here with TFs revealed that turning and licking are not best modulated by DLS, but rather by VMS and VLS, respectively. We note that DLS stimulation did cause licking and turning to some degree in our study. The behavioral phenotype caused by DLS stimulation reported in previous studies, as well as our own, might come from off-target stimulation of distant striatal regions (for example, VLS for licking and DMS for turning) that might have been exposed to scattered light. Overall, our work highlights the power of using TFs to map out striatal regions most effective at controlling specific behaviors.

The striatum is often described as functionally delineated along the medial–lateral axis, with DMS and DLS involved in goal-directed and habitual behaviors, respectively<sup>50</sup>. Our work suggests that this dichotomy might arise, partially, from distinct anatomical projections that underlie differential behavioral control. Interesting, many previous studies of DMS and DLS used lever-pressing tasks that require forelimb movement and locomotion. Thus, it is possible that goal-directed behavior and habitual behavior are two behavioral modes that specifically engage locomotion (DMS-based behavior) or forelimb motor sequences (DLS-based behavior), respectively, in a lever-press task.

Our work did not address functional segregation downstream of striatum (for example, SNr). Such segregation could be examined in different BG output nuclei by modulating distinct SNr neurons (for example, <sup>VLS</sup>SNr) during behavior, labeled with anterograde Cre delivery. Our anatomical work predicts that functional segregation is maintained throughout BG nuclei, and future experiments are necessary to test this prediction.

Complex behavioral sequences require brain circuits to ultimately integrate information across behavioral space. Our work suggests that BG might not be a site of integration, and that regions outside of the BG, such as cortex or SC, might serve this function.

### Online content

Any methods, additional references, Nature Research reporting summaries, source data, extended data, supplementary information, acknowledgements, peer review information; details of author contributions and competing interests; and statements of data and code availability are available at <https://doi.org/10.1038/s41593-020-00712-5>.

Received: 29 January 2020; Accepted: 21 August 2020;  
Published online: 28 September 2020

## References

- Roseberry, T. K. et al. Cell-type-specific control of brainstem locomotor circuits by basal ganglia. *Cell* **164**, 526–537 (2016).
- Kravitz, A. V. et al. Regulation of parkinsonian motor behaviours by optogenetic control of basal ganglia circuitry. *Nature* **466**, 622–626 (2010).
- Tai, L.-H., Lee, A. M., Benavidez, N., Bonci, A. & Wilbrecht, L. Transient stimulation of distinct subpopulations of striatal neurons mimics changes in action value. *Nat. Neurosci.* **15**, 1281–1289 (2012).
- Xiong, Q., Znamenskiy, P. & Zador, A. M. Selective corticostriatal plasticity during acquisition of an auditory discrimination task. *Nature* **521**, 348–351 (2015).
- Znamenskiy, P. & Zador, A. M. Corticostriatal neurons in auditory cortex drive decisions during auditory discrimination. *Nature* **497**, 482–485 (2013).
- Reynolds, J. N. J., Hyland, B. I. & Wickens, J. R. A cellular mechanism of reward-related learning. *Nature* **413**, 67–70 (2001).
- Shen, W., Flajolet, M., Greengard, P. & Surmeier, D. J. Dichotomous dopaminergic control of striatal synaptic plasticity. *Science* **321**, 848–851 (2008).
- Alexander, G. E., DeLong, M. R. & Strick, P. L. Parallel organization of functionally segregated circuits linking basal ganglia and cortex. *Annu. Rev. Neurosci.* **9**, 357–381 (1986).
- Deniau, J. M. & Chevalier, G. The lamellar organization of the rat substantia nigra pars reticulata: distribution of projection neurons. *Neuroscience* **46**, 361–377 (1992).
- Deniau, J. M., Menetrey, A. & Charpier, S. The lamellar organization of the rat substantia nigra pars reticulata: segregated patterns of striatal afferents and relationship to the topography of corticostriatal projections. *Neuroscience* **73**, 761–781 (1996).
- Kolomiets, B. P. et al. Segregation and convergence of information flow through the cortico-subthalamic pathways. *J. Neurosci.* **21**, 5764–5772 (2001).
- Kolomiets, B. P., Deniau, J. M., Glowinski, J. & Thierry, A. M. Basal ganglia and processing of cortical information: functional interactions between trans-striatal and trans-subthalamic circuits in the substantia nigra pars reticulata. *Neuroscience* **117**, 931–938 (2003).
- Kravitz, A. V., Tye, L. D. & Kreitzer, A. C. Distinct roles for direct and indirect pathway striatal neurons in reinforcement. *Nat. Neurosci.* **15**, 816–818 (2012).
- Yttri, E. A. & Dudman, J. T. Opponent and bidirectional control of movement velocity in the basal ganglia. *Nature* **533**, 402–406 (2016).
- Wang, L., Rangarajan, K. V., Gerfen, C. R. & Krausz, R. J. Activation of striatal neurons causes a perceptual decision bias during visual change detection in mice. *Neuron* **97**, 1369–1381.e5 (2018).
- Kelly, R. M. & Strick, P. L. Macro-architecture of basal ganglia loops with the cerebral cortex: use of rabies virus to reveal multisynaptic circuits. *Prog. Brain Res.* **143**, 447–459 (2004).
- Saunders, A. et al. A direct GABAergic output from the basal ganglia to frontal cortex. *Nature* **521**, 85–89 (2015).
- Jackson, A. & Crossman, A. R. Subthalamic nucleus efferent projection to the cerebral cortex. *Neuroscience* **6**, 2367–2377 (1981).
- Aoki, S. et al. An open cortico-basal ganglia loop allows limbic control over motor output via the nigrothalamic pathway. *eLife* **8**, e49995 (2019).
- Sippy, T., Lapray, D., Crochet, S. & Petersen, C. C. H. Cell-type-specific sensorimotor processing in striatal projection neurons during goal-directed behavior. *Neuron* **88**, 298–305 (2015).
- Babl, S. S., Rummell, B. P. & Sigurdsson, T. The spatial extent of optogenetic silencing in transgenic mice expressing channelrhodopsin in inhibitory interneurons. *Cell Rep.* **29**, 1381–1395.e4 (2019).
- Li, N. et al. Spatiotemporal constraints on optogenetic inactivation in cortical circuits. *eLife* **8**, e48622 (2019).
- Travers, J. B., Dinardo, L. A. & Karimnabazi, H. Motor and premotor mechanisms of licking. *Neurosci. Biobehav. Rev.* **21**, 631–647 (1997).
- Wang, S. & Redgrave, P. Microinjections of muscimol into lateral superior colliculus disrupt orienting and oral movements in the formalin model of pain. *Neuroscience* **81**, 967–988 (1997).
- Sahibzada, N., Dean, P. & Redgrave, P. Movements resembling orientation or avoidance elicited by electrical stimulation of the superior colliculus in rats. *J. Neurosci.* **6**, 723–733 (1986).
- Capelli, P., Pivetta, C., Esposito, M. S. & Arber, S. Locomotor speed control circuits in the caudal brainstem. *Nature* **551**, 373–377 (2017).
- Zingg, B. et al. AAV-mediated anterograde transsynaptic tagging: mapping corticocollicular input-defined neural pathways for defense behaviors. *Neuron* **93**, 33–47 (2017).
- Zingg, B., Peng, B., Huang, J., Tao, H. W. & Zhang, L. I. Synaptic specificity and application of anterograde transsynaptic AAV for probing neural circuitry. *J. Neurosci.* **40**, 3250–3267 (2020).
- Hunnicut, B. J. et al. A comprehensive excitatory input map of the striatum reveals novel functional organization. *eLife* **5**, e19103 (2016).
- Hintiryan, H. et al. The mouse cortico-striatal projectome. *Nat. Neurosci.* **19**, 1100–1114 (2016).
- Hooks, B. M. et al. Topographic precision in sensory and motor corticostriatal projections varies across cell type and cortical area. *Nat. Commun.* **9**, 1–16 (2018).
- Mastro, K. J., Bouchard, R. S., Holt, H. A. K. & Gittis, A. H. Transgenic mouse lines subdivide external segment of the globus pallidus (GPe) neurons and reveal distinct GPe output pathways. *J. Neurosci.* **34**, 2087–2099 (2014).
- Mana, S. & Chevalier, G. The fine organization of nigro-collicular channels with additional observations of their relationships with acetylcholinesterase in the rat. *Neuroscience* **106**, 357–374 (2001).
- Mandelbaum, G. et al. Distinct cortical-thalamic-striatal circuits through the parafascicular nucleus. *Neuron* **102**, 636–652.e7 (2019).
- Klapoetke, N. C. et al. Independent optical excitation of distinct neural populations. *Nat. Methods* **11**, 338–346 (2014).
- Kuramoto, E. et al. Ventral medial nucleus neurons send thalamocortical afferents more widely and more preferentially to layer 1 than neurons of the ventral anterior–ventral lateral nuclear complex in the rat. *Cereb. Cortex* **25**, 221–235 (2015).
- Rubio-Garrido, P., Pérez-de-Manzo, F., Porrero, C., Galazo, M. J. & Clascá, F. Thalamic input to distal apical dendrites in neocortical layer 1 is massive and highly convergent. *Cereb. Cortex* **19**, 2380–2395 (2009).
- Krout, K. E., Loewy, A. D., Westby, G. W. M. & Redgrave, P. Superior colliculus projections to midline and intralaminar thalamic nuclei of the rat. *J. Comp. Neurol.* **431**, 198–216 (2001).
- McHaffie, J. G., Stanford, T. R., Stein, B. E., Coizet, V. & Redgrave, P. Subcortical loops through the basal ganglia. *Trends Neurosci.* **28**, 401–407 (2005).
- Chevalier, G. & Deniau, J. M. Spatio-temporal organization of a branched tecto-spinal/ tecto-diencephalic neuronal system. *Neuroscience* **12**, 427–439 (1984).
- Oh, S. W. et al. A mesoscale connectome of the mouse brain. *Nature* **508**, 207–214 (2014).
- Rossi, M. A. et al. A GABAergic nigroretectal pathway for coordination of drinking behavior. *Nat. Neurosci.* **19**, 742–748 (2016).
- Evans, D. A. et al. A synaptic threshold mechanism for computing escape decisions. *Nature* **558**, 590–594 (2018).
- Shang, C. et al. A parvalbumin-positive excitatory visual pathway to trigger fear responses in mice. *Science* **348**, 1472–1477 (2015).
- Pisano, F. et al. Depth-resolved fiber photometry with a single tapered optical fiber implant. *Nat. Methods* **16**, 1185–1192 (2019).
- Pisanello, M. et al. Tailoring light delivery for optogenetics by modal demultiplexing in tapered optical fibers. *Sci. Rep.* **8**, 4467 (2018).
- Pisanello, F. et al. Dynamic illumination of spatially restricted or large brain volumes via a single tapered optical fiber. *Nat. Neurosci.* **20**, 1180–1188 (2017).
- Gong, S. et al. Targeting Cre recombinase to specific neuron populations with bacterial artificial chromosome constructs. *J. Neurosci.* **27**, 9817–9823 (2007).
- Tecuapetla, F., Matias, S., Dugue, G. P., Mainen, Z. F. & Costa, R. M. Balanced activity in basal ganglia projection pathways is critical for contraversive movements. *Nat. Commun.* **5**, 4315 (2014).
- Yin, H. H. & Knowlton, B. J. The role of the basal ganglia in habit formation. *Nat. Rev. Neurosci.* **7**, 464–476 (2006).

**Publisher's note** Springer Nature remains neutral with regard to jurisdictional claims in published maps and institutional affiliations.

© The Author(s), under exclusive licence to Springer Nature America, Inc. 2020

## Methods

**Mice.** All mouse handling and manipulations were performed in accordance with protocols approved by the Harvard Standing Committee on Animal Care, following guidelines described in the US National Institutes of Health Guide for the Care and Use of Laboratory Animals. For anatomical tracing, male and female *Rosa26-Lox-STOP-Lox-H2B-EGFP* and wild-type (C57BL/6NcrJ, Charles River) mice (age > postnatal day (P) 60) were used. For slice physiology, we used male wild-type mice (C57BL/6NcrJ, Charles River, age > P56). For behavioral experiments, we used *Drd1a-Cre* (B6.FVB(Cg)-Tg(Drd1-cre)EY262Gsat/Mmucd, 030989-UCD) on C57BL/6J backgrounds acquired from Mutant Mouse Resources & Research Centers (MMRRC) UC Davis. For in vivo validation of TFs, we used *Adora2a-Cre* (B6.FVB(Cg)-Tg(Adora2a-cre)KG139Gsat/Mmucd, 036158-UCD) from MMRRC UC Davis. For the dopamine axons validation experiment, *Slc6a3-IRES-Cre* mice were obtained from the Jackson Laboratory (stock number 006660). All mice were housed on a 12-h dark/12-h light reversed cycle. Behavioral mice performed the task during the dark cycle.

**Surgery.** Isoflurane (2.5% in 80% oxygen) was used to anaesthetize mice. Under the stereotaxic frame (David Kopf Instruments, model 1900), the skull was exposed and leveled (David Kopf Instruments, model 1905). A ~300- $\mu$ m-diameter craniotomy was made with a drill (David Kopf Instruments, model 1911) for each viral injection. Viruses were injected through a pulled glass pipette (Drummond Scientific Company) using a syringe pump (Harvard Apparatus, model 84850). Viruses were drawn into the pipette at a rate of 500 nl min<sup>-1</sup> then slowly lowered into the target region. Pipettes were first lowered 300  $\mu$ m deeper than the target dorsoventral coordinates and raised back up to the target coordinates to minimize back spill through the pipette track. The pipette was left in the brain for 5 min before injection began. The injection rate was <75 nl min<sup>-1</sup>. After infusion, the pipette was left in place for another 5 min before it was slowly withdrawn. For fiber implants, a stereotaxic cannula holder (SCH\_1.25, Doric) was used to hold the fiber and the fiber was slowly lowered into the brain. The fiber and headpost were secured on the skull using Loctite gel (McMaster-Carr 74765A65) and Zip Kicker (Pacer Technology). Mice were given pre- and postoperative oral carprofen (MediGel CPF, 5 mg kg<sup>-1</sup> d<sup>-1</sup>) as an analgesic, and monitored for at least 5 d.

**Anatomical tracing.** All coordinates written as anterior/medial/lateral/dorsoventral (AP/ML/DV) are in millimeters and given as from bregma (AP and ML) and dura (DV). For mapping topography from striatum to EP, GPe and SNr, AAV2/1-hSyn-Cre (titer:  $1 \times 10^{13}$  genome copies (gc) ml<sup>-1</sup>, University of Pennsylvania Vector Core or Addgene AV-1-PV2676) was focally injected (volume: ~75 nl, rate: 50 nl min<sup>-1</sup>) into DMS, DLS or VLS in H2B-EGFP reporter mice. Coordinates for striatal regions were as follows: DMS, +0.5/+1.25/-2.2; DLS, +0.5/+2.2/-2.1; and VLS, +0.5/+2.25/-3. To avoid going through DLS when injecting in VLS, we drilled a hole at +0.5/+3.4 (AP/ML) and advanced 3.35 mm (from dura) at 14.5 degrees relative to the midline. This minimized viral leak into DLS when injecting into VLS. Two weeks after the injection, mice were perfused. For mapping topography of medial/lateral striatum to EP, GPe and SNr, ~100 nl of AAV2/1-hSyn-Cre (same as above) and AAV2/1-hSyn-Flpo (Plasmid from Addgene no. 60663, packaged in Boston Children Hospital Viral Core, titer:  $7.9 \times 10^{12}$  gc ml<sup>-1</sup>) were injected into medial striatum (+0.5/+1.25/-2.2) or lateral striatum (+0.5/+2.5/-2.3), respectively. This was followed by an injection of a ~400-nl mixture (1:1) of AAV2/1-FLEX-TdTom (University of Pennsylvania Vector Core, titer:  $5 \times 10^{12}$  gc ml<sup>-1</sup>) and AAV2/1-Efla-fDIO-EYFP (Addgene no. 55641, packaged in Boston Children Hospital Viral Core, titer:  $4 \times 10^{12}$  gc ml<sup>-1</sup>) into EP (-1.22/+1.8/-3.8), GPe (-0.4/+1.8/-3.5) or SNr (-3.2/+1.5/-4.5). Four weeks after the injection, mice were perfused. For mapping focal topography from SNr to output regions, ~75 nl of AAV2/1-hSyn-Cre (same as above, titer:  $1 \times 10^{13}$  gc ml<sup>-1</sup>) was injected into DMS, DLS or VLS (coordinates as above). This was followed by an injection of AAV2/1-FLEX-TdTom (same as above, titer:  $1 \times 10^{13}$  gc ml<sup>-1</sup>) into SNr. Mice were perfused 4 weeks after injection. For mapping the output of SNr recipient VM, 400 nl of AAV2/1-hSyn-Cre was injected in SNr (same as above), followed by AAV2/1-CAG-FLEX-EGFP (University of Pennsylvania Vector core, titer:  $8 \times 10^{11}$ ) into VM (-1.4/+0.8/-4.5). Mice were perfused 4 weeks after injection. For mapping VM topography, ~100 nl of CTB (Recombinant) Alexa Fluor (488, 555 or 647 conjugate, Thermo Scientific) was injected into the superficial cortex of tJM1 (+2.5/+2/-0.25), fM1 (+1/+1.7/-0.25) or ACA (angled injection, +0.5/+1/advanced -1.4 at 45 degrees) in the same mouse. Mice were perfused 1 week after injection. For mapping SC topography, ~150 nl of AAV2/1.hSyn.Cre and AAV2/1.hSyn.Flpo were injected into tJM1 and ACA, respectively (same coordinates as above), followed by 100 nl of AAV2/1.Efla.fDIO.EYFP in lateral SC (-3.4/+1.5/-2.1, titer same as above) or AAV2/1.FLEX.TdTom in medial SC (-3.4/+0.5/-1.8, titer same as above). For validating dopaminergic-negative SNr projection, 200 nl of AAV1.Flpo was injected into striatum (+0.5/+2.0/-2.5), and a 200-nl mixture of AAV2/1.FLEX.TdTom (titer:  $5 \times 10^{12}$  gc ml<sup>-1</sup>) and AAVDJ.hSyn.Coff/Fon.EYFP (the Vector Core at the University of North Carolina at Chapel Hill (UNC vector core), titer:  $3.4 \times 10^{12}$  gc ml<sup>-1</sup>) was injected into SNr/SNc (-3.2/+1.5/-4.5).

**Slice physiology.** Slice physiology was performed similar to that previously described<sup>24</sup>. Briefly, mice were anesthetized by isoflurane inhalation and perfused

transcardially with ice-cold artificial cerebrospinal fluid (ACSF) consisting of: 125 mM NaCl, 2.5 mM KCl, 25 mM NaHCO<sub>3</sub>, 2 mM CaCl<sub>2</sub>, 1 mM MgCl<sub>2</sub>, 1.25 mM NaH<sub>2</sub>PO<sub>4</sub> and 11 mM glucose (300–305 mOsm kg<sup>-1</sup>). Then, 300- $\mu$ m coronal slices were cut in ice-cold ACSF and transferred for 10 min to a holding chamber at 34 °C containing choline-based solution (110 mM choline chloride, 25 mM NaHCO<sub>3</sub>, 2.5 mM KCl, 7 mM MgCl<sub>2</sub>, 0.5 mM CaCl<sub>2</sub>, 1.25 mM NaH<sub>2</sub>PO<sub>4</sub>, 25 mM glucose, 11.6 mM ascorbic acid and 3.1 mM pyruvic acid). Slices were then transferred to a second 34 °C temperature chamber with ACSF for at least 30 min. The chamber was moved to room temperature for the duration of the experiment. Recordings were performed at 32 °C with a flow of 2–3 ml min<sup>-1</sup> carbogen-bubbled ACSF. We used patch pipettes (2.5–3.5 M $\Omega$ ) pulled from borosilicate glass (Sutter Instruments). Cesium-based internals were used to voltage clamp experiments: 135 mM CsMeSO<sub>4</sub>, 10 mM HEPES, 1 mM EGTA, 3.3 mM QX-314 (Cl<sup>-</sup> salt), 4 mM Mg<sup>2+</sup> ATP, 0.3 mM Na-GTP, 8 mM Na<sub>2</sub>-phosphocreatine, pH 7.3 adjusted with CsOH; 295 mOsm kg<sup>-1</sup>. Slices were obtained that contained CTB-labeled cells in either Pf or VM. Only slices where CTB of both colors along with CoChR axon fibers were present were used for experiments. Mice that lacked at least one of these features were discarded in the analysis. This was to ensure fair comparison across different CTB-colored cells. Stimulation consisting of a 3-ms pulse (4–6 mW) was used to activate CoChR-expressing axons.

**TF optical setup and calibration.** An optical setup allowed us to direct the laser beam onto the patchcord at different incident angles (Extended Data Fig. 9). A custom MATLAB script was used to control the galvo mirror for controlling the incident angle, and a piezo mirror far from the galvo mirror to correct the position of the beam onto the back of the patchcord due to minor misalignment. Power was controlled via a pockels cell (Conoptics) and calibrated such that light coming out of the patchcord was the same for all galvo mirror angles. A 0.66-NA patchcord (Plexon) and 0.66-NA TFs (2-mm emitting length, 2.5-mm implant length, Optogenix) were used for all our behavioral experiments.

**TF in vivo validation and recording analysis.** For characterizing the resolution of TF illumination, TF was immersed inside fluorescein solution. Fluorescent images of the TF illumination were acquired using a widefield microscope under a 2x objective (VS120, OLYMPUS) with OlyVIA. For validating the use of TF in vivo, a custom TF with 2.5-mm emitting length and 5-cm implant length (Optogenix) was attached parallel to a one-shank silicon probe (A1x32-Edge-5mm-100-177, NeuroNexus). Distance between the TF tip and the probe was ~300  $\mu$ m. Attaching the TF too close to the probe resulted in low recording yield. For in vivo validation, *Adora2a-Cre* mice were injected with AAV2/9.Syn.FLEX.CoChR.GFP into the entire striatum (300 nl at +0.8/+2/-3.2 and 300 nl at +0.8/+2/-2, total volume: 600 nl). Two weeks following injection, a small craniotomy was made above the injection site and acute recording was performed (see section “Extracellular recording and analysis”). Power for each depth illumination was calibrated to ~50  $\mu$ W at the tip of the patchcord. Each depth was stimulated randomly every ~5–10 s, at a constant pulse of 1-s duration. For analysis, units within a 200- $\mu$ m region (two consecutive channel sites) were combined (Fig. 5e). To look at the resolution of the stimulation, firing rate for individual units was normalized to the peak firing rate, and the change in firing rate relative to baseline was computed (Fig. 5e).

**Behavioral experiments and stimulation.** For investigating licking behavior, we designed a lateralized licking task similar to a previous study<sup>21</sup>. After surgery and full recovery, mice were water deprived until they reached 90% of their baseline weight. Mice were first habituated for head-fixation on the behavioral rig. On the habituation day, mice were given free water from one of the two spouts initially positioned in front of the mouth. As soon as mice became comfortable with licking for water rewards, mice were trained to withhold licking until a short tone (50-ms duration, 6 kHz, Arduino tone function) was played, after which licking within 0.5 s (response window) after the tone dispensed a small water reward. Initially, mice had to withhold licking for ~1–2 s (intertrial interval). Licking during this interval reset the clock and mice had to further wait the same amount of time. Once mice learned to lick only to tone, they were further trained to lick left or lick right after presentation of tone A (6 kHz) or tone B (12 kHz), respectively. Tones were presented in blocks initially (50 trials with only one tone type) for ~2–4 d. Once mice learned to respond well to tones and to lick sideways, tones were presented randomly with ~2–4-s intertrial interval. Not licking to either side of the spout during the response window led to a ‘miss trial’ and a timeout period (6 s), during which tones were not played. Training on the final task continued either until the mouse achieved 90% accuracy or for 2 weeks. Once mice were fully trained, optogenetic stimulation was delivered via a setup capable of delivering an angled laser beam on the back of the patchcord. Stimulation consisted of a 100- $\mu$ W, 473-nm constant light pulse of 100 ms duration (measured at the patchcord) delivered either during tone (25 ms after tone onset) or during the inter-trial interval (randomly 1.5–3.5 s after the last lick) on 20% of all trials to minimize stimulation-induced learning/plasticity. Only one fiber was simulated per session, and each fiber was stimulated over two sessions.

For open field behavior, the same mice that underwent training on the licking task were put in a white rectangular chamber. Stimulation consisted of a 0.8-s constant pulse at 100  $\mu$ W delivered randomly every ~10–15 s. Each fiber was

stimulated through separate sessions and stimulation sites were randomized within sessions. Animals were monitored through a camera (Pointgrey) positioned above the chamber, using FlyCapture2, and nose/body positions were extracted post hoc through EthoVision XT.

**Histology analysis.** For all anatomy experiments, injected mice were euthanized and perfused transcardially with PBS followed by 4% PFA. After 24-h post-fix in 4% PFA, brains were equilibrated in 30% sucrose solution until they sank to the bottom. Brains were then sliced (50  $\mu\text{m}$  thick) using a cryostat, mounted on glass slides and imaged under a widefield microscope with a 10x objective (VS120, OLYMPUS). Images were acquired through OlyVIA 2.9.

For mapping topography from striatum to BG output nuclei, an anterior–posterior position was chosen from the Paxinos atlas for each type of nuclei (GPe:  $-0.34$  mm, EP:  $-1.34$  mm, SNr:  $-3.52$ , all from Bregma in mm). Histology sections that best matched the atlas were chosen for analysis. Positions of the anterogradely labeled cells expressing H2B-EGFP were detected through ImageJ. A map of cell density per area was quantified for each mouse, then normalized via peak density in that mouse. The normalized density map for each mouse was then averaged and plotted (Fig. 1d). For quantifying relative intensity, 15 regions of putative SNr targets were preselected based on previous single-neuron tracing, combined with observation from histological slices<sup>52</sup>. A region of interest ( $400 \times 400 \mu\text{m}^2$ ) was drawn around the target region representing the putative target, and average fluorescence intensity was calculated. Final intensity values were normalized by the total sum of average fluorescence intensity in all 15 regions, yielding a normalized relative fluorescence intensity (Extended Data Fig. 6b).

For behavioral mice, striatal slices were immune-stained against glial fibrillary acidic protein (GFAP, 1:500 dilution, Agilent Technologies, Z033429-2) to verify the location of the fiber implants (Fig. 6b).

**Behavioral analysis.** For mapping the lick-related striatal region after dSPN stimulation during the ITI, licking probability was defined as the probability that mice would lick within a 500-ms window after laser onset (Fig. 6f). Trained mice rarely licked within this inter-trial interval. Mean contra or ipsi licking probabilities across sessions were calculated for DMS, DLS and VLS. A separate bootstrap analysis was performed for calculating *P* values across all stimulated regions. Hierarchical bootstrapping was done to test the likelihood of obtaining the experimentally observed probability of licking by chance. Null distribution was calculated by resampling with replacement the mice, sessions and shuffled trial type (stimulation versus no-stimulation trials)  $10^5$  times. One-sided *P* values were defined as the likelihood of obtaining a probability of licking (ipsi and contra combined) higher than the actual probability, under the null hypothesis that stimulation did not cause licking (stim and no stim trials shuffled). For mapping the striatal region sufficient to interfere with ongoing licking, we ran a similar bootstrap analysis, where null distribution was calculated by resampling with replacement the mice, sessions and shuffled trial type (stim versus no stim)  $10^5$  times. One-sided *P* values were the likelihood of observing a lower correct trial rate than the experimental value observed, under the null hypothesis that stimulation did not interfere with licking (stim and no stim trials shuffled).

For mapping the turning-related striatal region, we quantified the  $\Delta\text{turn}$  angle by computing the cumulative turned angle relative to the angle at time relative to laser onset  $t = 0$  from laser onset (Fig. 8c). For testing statistical significance, we computed  $\Delta\text{turn}^{\text{stim}} - \Delta\text{turn}^{\text{baseline}}$ , defined as the angle turned during stimulation ( $-800$  ms relative to laser onset) minus the angle turned before stimulation ( $-800$  to  $0$  ms relative to laser onset) (Fig. 8d,e). This was done to remove any general turning bias that the mouse might have. A positive angle was defined as turning contralateral to the fiber location. Hierarchical bootstrapping was done to test the null hypothesis that stimulation did not induce any more turning than would be expected by chance. We resampled  $10^5$  times, with replacement, mice and stimulation trials. For bootstrapping, we used the median value across all trials for each mouse and computed the mean across mice. One-sided *P* values were defined as the likelihood of finding an instance with  $\Delta\text{turn}^{\text{stim}} - \Delta\text{turn}^{\text{baseline}} < 0$ , meaning that stimulation caused ipsilateral turn, contrary to what was observed. All analyses were implemented using MATLAB and Excel.

**Extracellular recording and analysis.** Mice for in vivo recording underwent a similar surgery to those used for TF stimulation, but with an additional craniotomy performed above tJM1 ( $+2.5/+2.0/0$ ) and lateral SC ( $-3.4/+1.5/0$ ) 1 day before the recording session. Mice were first trained on the main task, and then it was confirmed that stimulation in VLS induced the licking phenotype, before undergoing craniotomy surgery and subsequent recording. Each mouse had two craniotomies, one above tJM1 and one above SC. Recording sessions alternated between these two sites and were done over  $\sim 2$  weeks. Electrophysiological recordings were conducted in a similar way as described before<sup>53</sup>. Briefly, recordings were conducted using 64-channel probes with two-shank arrays (A2x32-5mm-25-200-177, NeuroNexus Technologies). Probes were lowered until they reached a target depth (tJM1:  $-1,000 \mu\text{m}$ , SC:  $-2,500 \mu\text{m}$ , relative to dura) and

units could be observed. Recording was done using Omniplex software (Plexon), and spikes were sorted manually using Offline Sorter (Plexon).

We quantified the mean firing rate across all units for tJM1 and ISC aligned to tone onset or laser onset (Extended Data Fig. 10). For quantifying the proportion of cells that were significantly changed by the stimulation, we counted the number of spikes within a 500-ms window after the relevant event (laser onset for stimulation, dummy control timestamp for control trials), and used two-sided Mann–Whitney *U*-test. Cells with *P* values  $< 0.05$  were classified as significantly changed after stimulation, and were further categorized into excited or inhibited depending on the direction of change (Extended Data Fig. 10c). Firing rates were smoothed using a Gaussian kernel (20 ms window) for display purposes.

**Statistical analyses.** All statistical analyses were performed using custom code written in MATLAB (MathWorks). For slice physiology (Figs. 3d and 4f), we used one-sided Mann–Whitney *U*-test. For mapping the striatal region effective at driving licking or turning, we used hierarchical bootstrapping (see the “Behavioral analysis” section). For quantifying the number of cells that were significantly modulated by dSPN stimulation, we used two-sided Mann–Whitney *U*-test. The significance level was not corrected for multiple comparisons. No statistical methods were used to predetermine sample sizes, but our sample sizes are similar to those reported in previous publications. Data distribution was assumed to be normal, but this was not formally tested. We used nonparametric tests for all analyses.

**Reporting summary.** Further information on the research methods relevant for this study is available in the Nature Research Reporting Summary.

## Data availability

The data that support the findings of this study are available from the corresponding author upon reasonable request.

## Code availability

The code used for analysis (MATLAB) is also available from the corresponding author upon reasonable request. Detailed information about software and methods used is available online in the Nature Research Reporting Summary.

## References

- Guo, Z. V. et al. Flow of cortical activity underlying a tactile decision in mice. *Neuron* **81**, 179–194 (2014).
- Cebrián, C., Parent, A. & Prensa, L. Patterns of axonal branching of neurons of the substantia nigra pars reticulata and pars lateralis in the rat. *J. Comp. Neurol.* **492**, 349–369 (2005).
- Oldenburg, I. A. & Sabatini, B. L. Antagonistic but not symmetric regulation of primary motor cortex by basal ganglia direct and indirect pathways. *Neuron* **86**, 1174–1181 (2015).

## Acknowledgements

We thank members of the Sabatini laboratory, W. Regehr, M. Andermann and N. Uchida for discussions. We thank J. Levasseur for mouse husbandry and genotyping, and J. Saulnier and L. Worth for laboratory administration. We thank W. Kuwamoto, J. Grande, M. Ambrosino, B. Pryor and E. Lubbers for assistance with behavioral experiments and histology. This work was supported by the NIH (grant no. NINDS R01NS103226), a P30 Core Center Grant (grant no. NINDS NS072030), an Iljoo Foundation scholarship and a grant from the Simons Collaborative on the Global Brain.

## Author contributions

J.L. and B.L.S. conceptualized the study, wrote the original draft, and reviewed and edited the manuscript. J.L. performed and participated in all experiments and W.W. performed the slice electrophysiology experiments. B.L.S. supervised the study and was responsible for acquisition of funding.

## Competing interests

B.L.S. is a founder of and holds private equity in Optogenix. Tapered fibers commercially available from Optogenix were used as tools in the research.

## Additional information

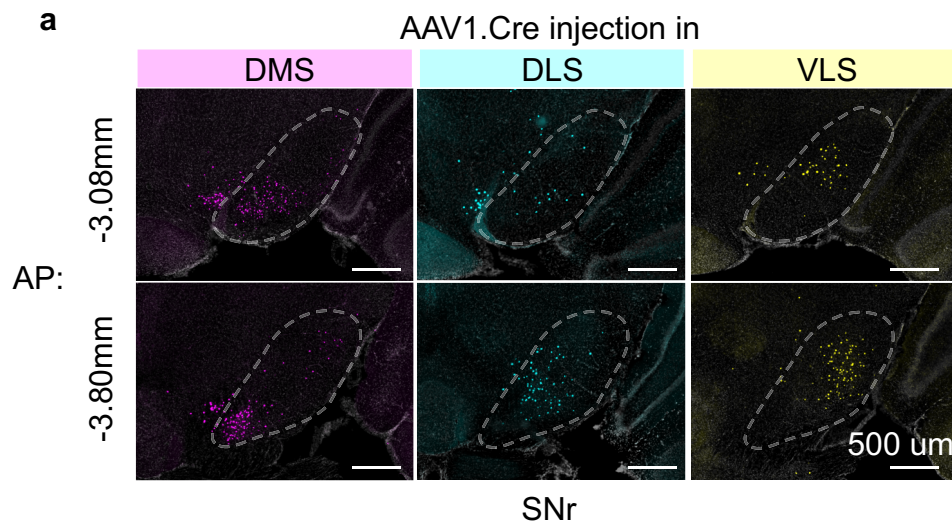
**Extended data** is available for this paper at <https://doi.org/10.1038/s41593-020-00712-5>.

**Supplementary information** is available for this paper at <https://doi.org/10.1038/s41593-020-00712-5>.

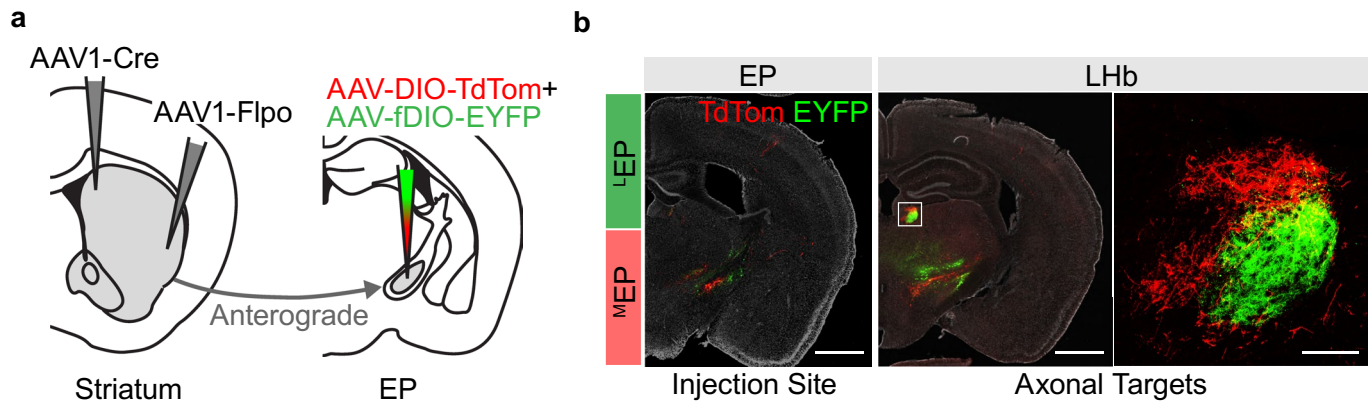
**Correspondence and requests for materials** should be addressed to B.L.S.

**Peer review information** *Nature Neuroscience* thanks Marc Fuccillo and the other, anonymous, reviewer(s) for their contribution to the peer review of this work.

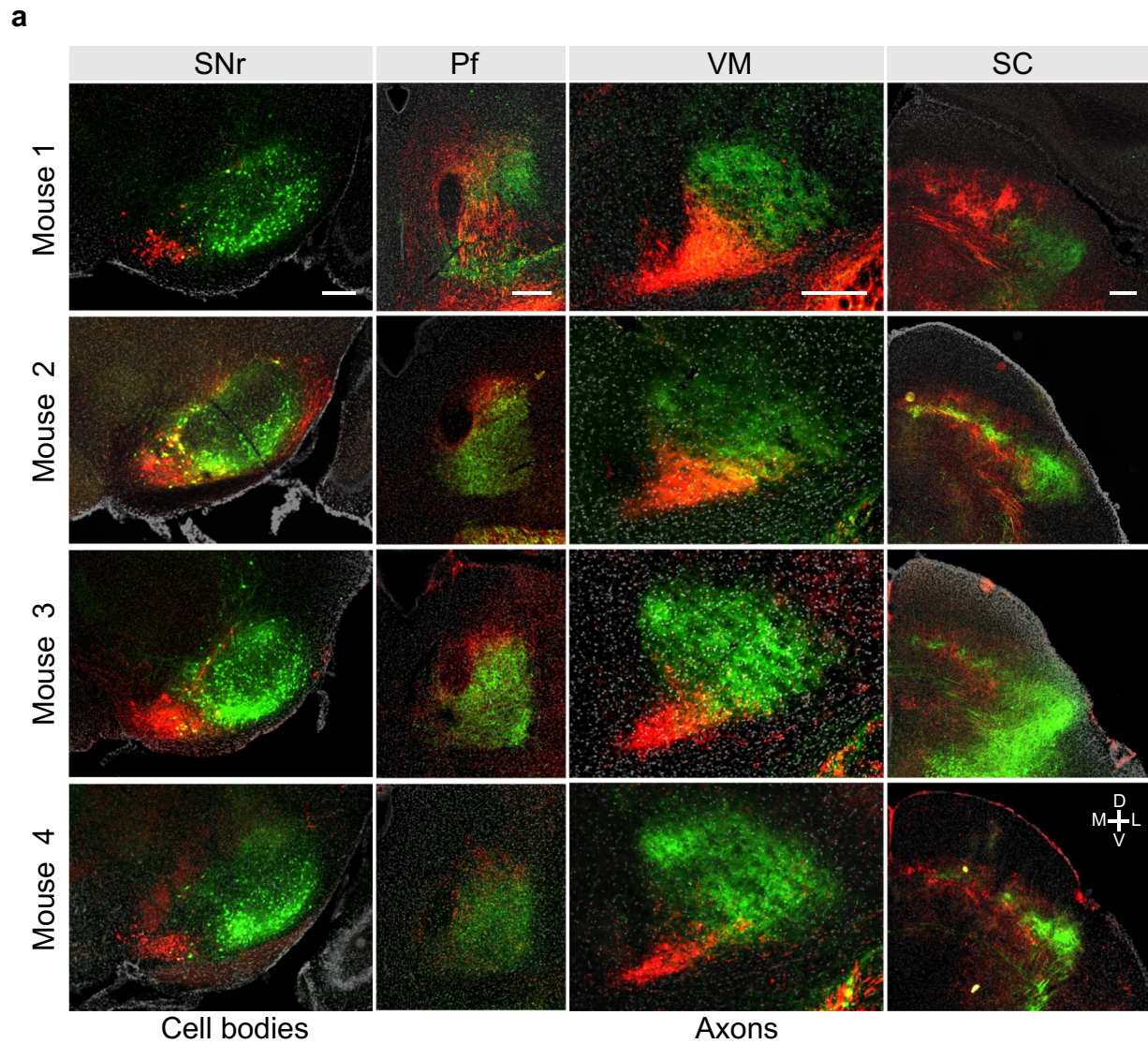
**Reprints and permissions information** is available at [www.nature.com/reprints](http://www.nature.com/reprints).



**Extended Data Fig. 1 | Topography is maintained across the AP axis of SNr.** **a**, Example histology section in anterior SNr and posterior SNr (see main text and methods for injection protocol). Row represent AP coordinates and each column indicates the location of the AAV1.cre for anterograde tracing (see main text). Scale bar, 500 $\mu$ m. Topographical labelling was also observed in anterior part of SNr. Similar results were obtained in  $n = 9$  mice ( $n = 3$  for each site).

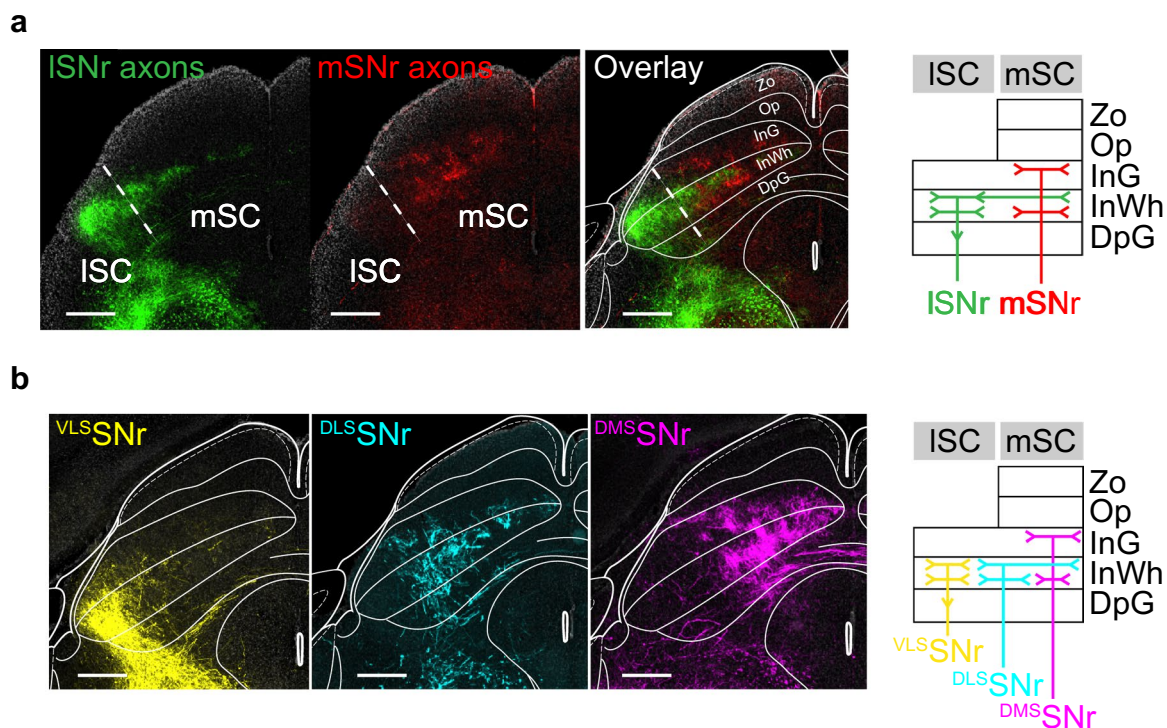


**Extended Data Fig. 2 | EP to LHb projection is topographic.** **a**, Experiment protocol. AAV1-cre and AAV1-Flpo in medial and lateral striatum respectively, followed by a cocktail of viruses encoding either DIO-TdTom or fDIO-EYFP in EP. **b**, *left*, histological sections showing the anterogradely labelled cells from medial (red) and lateral (green) striatum. *right*, Axonal fibers innervating LHb in a non-overlapping fashion. Similar results were obtained in  $n = 2$  mice. Scale bar, 1mm, 1mm, 0.1mm from left to right panel.

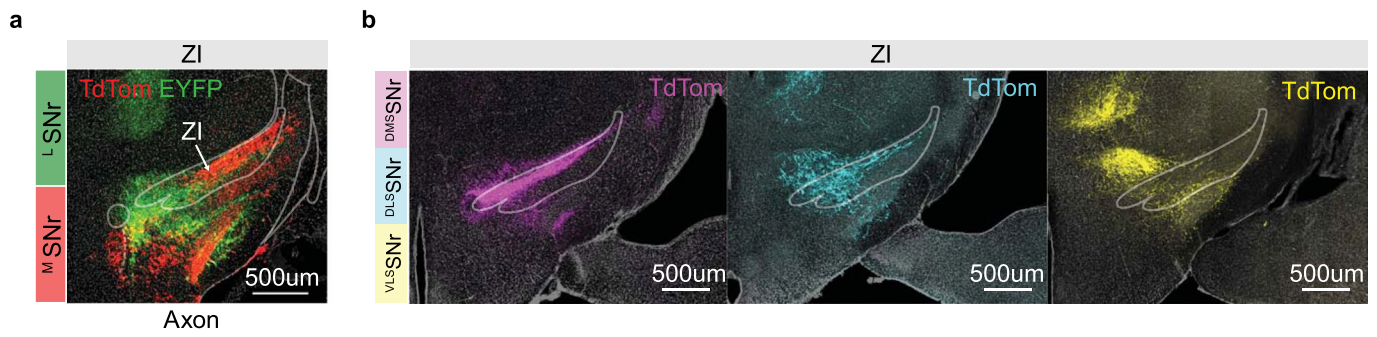


**Extended Data Fig. 3 | Topography of SNr output is consistent across mice.** **a**, Histology sections for all injected mice for experiment in Fig. 2c. First row represents column the injection site, and second to fourth column represent axonal fibers in Pf, VM and SC. Each row represents individual mouse. Scale bar, 250um.

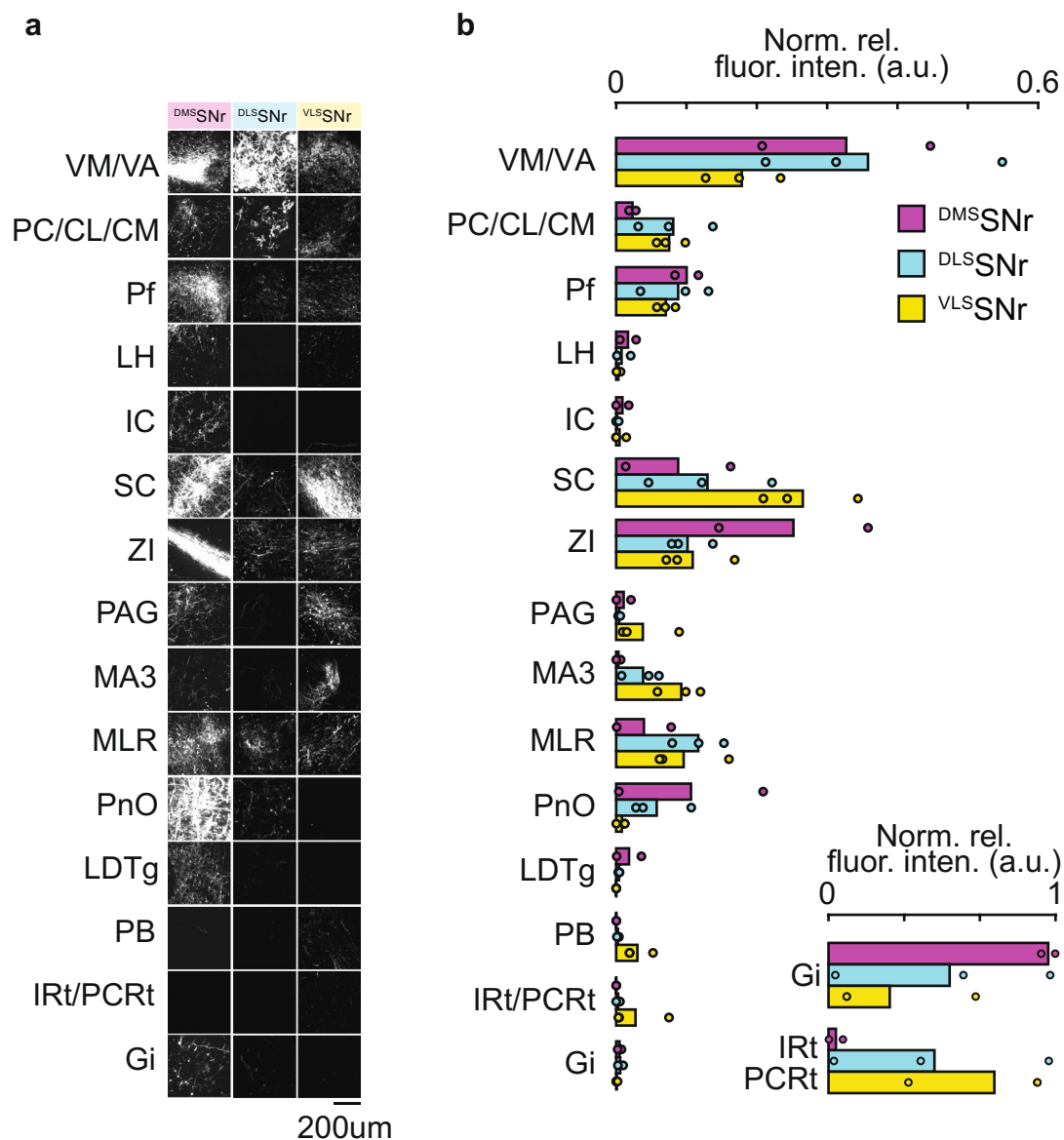




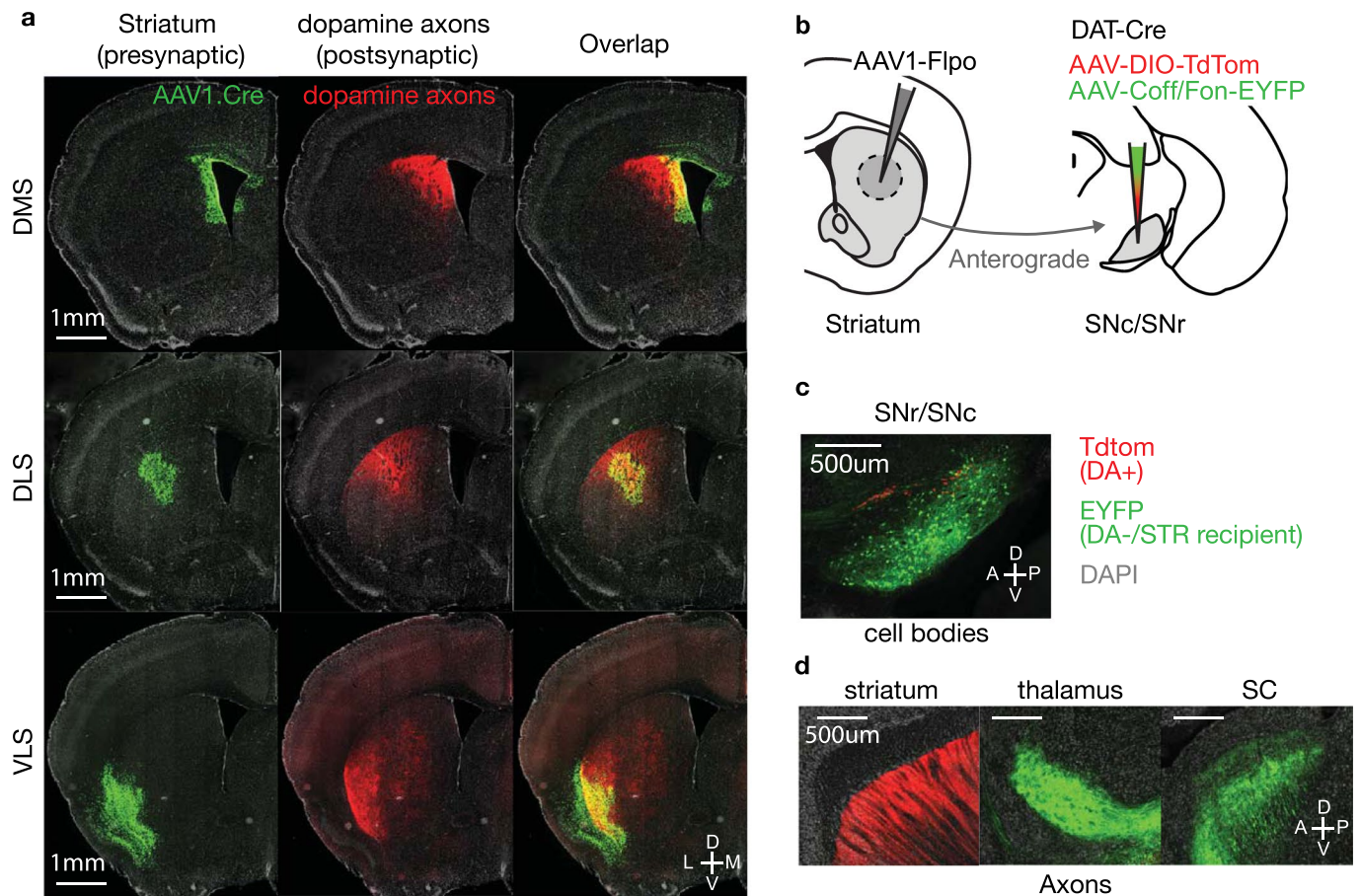
**Extended Data Fig. 4 | SNr output to SC segregated both across medial-lateral axis and across layers.** **a**, *left*, Example histology section with mSNr axons (red) and ISNr axons (green) from experiment described in Fig. 2c. *right*, Cartoon diagram summarizing the region and layer specificity of ISNr and mSNr observed. ISNr innervated the lateral SC (abbreviations: **Zo**: Zona layer of the superior colliculus, **Op**: optic nerve layer of the superior colliculus, **InG**: Intermediate gray layer of the superior colliculus, **InWh**: Intermediate white layer of the superior colliculus, **DpG**: Deep gray layer of the superior colliculus). ISNr innervated the ISC in InWh, and extending to upper layer of InWh in mSC. mSNr innervated the superficial part of InG and deeper part of InWh in mSC. Similar results were obtained in  $n = 4$  mice. Scale bar, 500um. **b**, *left*, Example histological section with <sup>VLS</sup>SNr (yellow), <sup>DLS</sup>SNr (cyan), and <sup>DMS</sup>SNr (magenta) axons in SC (images reproduced from Fig. 2f). *right*, Cartoon diagram summarizing the region and layer specificity of <sup>VLS</sup>SNr, <sup>DLS</sup>SNr, and <sup>DMS</sup>SNr observed. <sup>VLS</sup>SNr targeted the InWh part of ISC, <sup>DLS</sup>SNr targeted the central part of SC, extending to the upper layer of InWh in mSC, and <sup>DMS</sup>SNr targeted the upper InG and the lower InWh. Thus, ISNr axons seem to be a combination of <sup>VLS</sup>SNr and <sup>DLS</sup>SNr. Scale bar, 500um. Similar results were obtained in  $n = 9$  mice, 3 for each site.



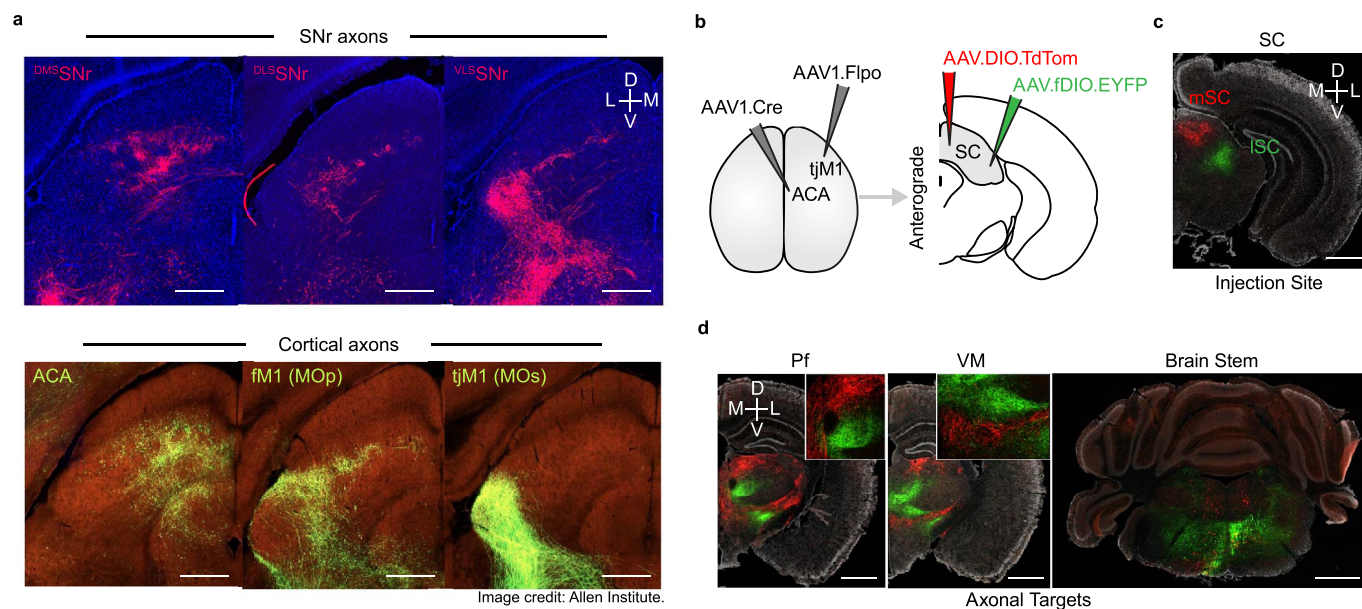
**Extended Data Fig. 5 | SNr output to Zona Incerta is topographically organized.** **a**, Example coronal section showing mSNr (red:TdTom) and lSNr (green:EYFP) axon fibers in zona incerta, from experiment described in Fig. 2a. Similar results were obtained in  $n = 4$  mice. **b**, Example coronal sections showing  $^{DMS}$ SNr (magenta:TdTom),  $^{DL}$ SNr (cyan:TdTom) and  $^{VL}$ SNr (yellow:TdTom), axon fibers in zona incerta, from experiment described in Fig. 2e. Similar results were obtained in  $n = 9$  mice,  $n = 3$  for each site.



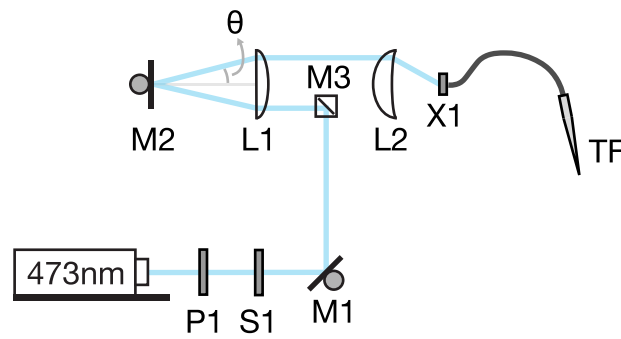
**Extended Data Fig. 6 | Brain regions targeted by SNr.** **a**, Example histology section of brain regions targeted by <sup>DMS</sup>SNr, <sup>DLS</sup>SNr, and <sup>VLS</sup>SNr. Each row represent a brain region, and each column is a different SNr subpopulation labelled from distinct striatal regions (see experiment described in Fig. 2e). **b**, *top left*, Quantification of normalized fluorescence intensity across brain regions for <sup>DMS</sup>SNr, <sup>DLS</sup>SNr, and <sup>VLS</sup>SNr (see Methods). *bottom right*, Similar quantification of brain stem regions, IRt and PCRt, but normalized only to total fluorescence in brain stem. Abbreviations. **VM/VA**: ventromedial/ventral anterior thalamus, **PC/CL/CM**: paracentral/centrolateral/central medial thalamus, **Pf**: parafascicular nucleus, **LH**: lateral hypothalamus, **IC**: inferior colliculus, **SC**: superior colliculus, **ZI**: zona incerta, **PAG**: paracqeuoductal gray, **MA3**: medial accessory oculomotor nucleus, **MLR**: mesencephalic locomotor region, **PnO**: pontine reticular nucleus, oral part, **LDTg**: laterodorsal tegmental nucleus, **PB**: parabrachial nucleus, **IRt**: intermediate reticular nucleus, **PCRt**: parvicellular reticular nucleus, **Gi**: gigantocellular reticular nucleus (<sup>DMS</sup>SNr: n=2 mice; <sup>DLS</sup>SNr: n=3 mice; <sup>VLS</sup>SNr: n=3 mice).



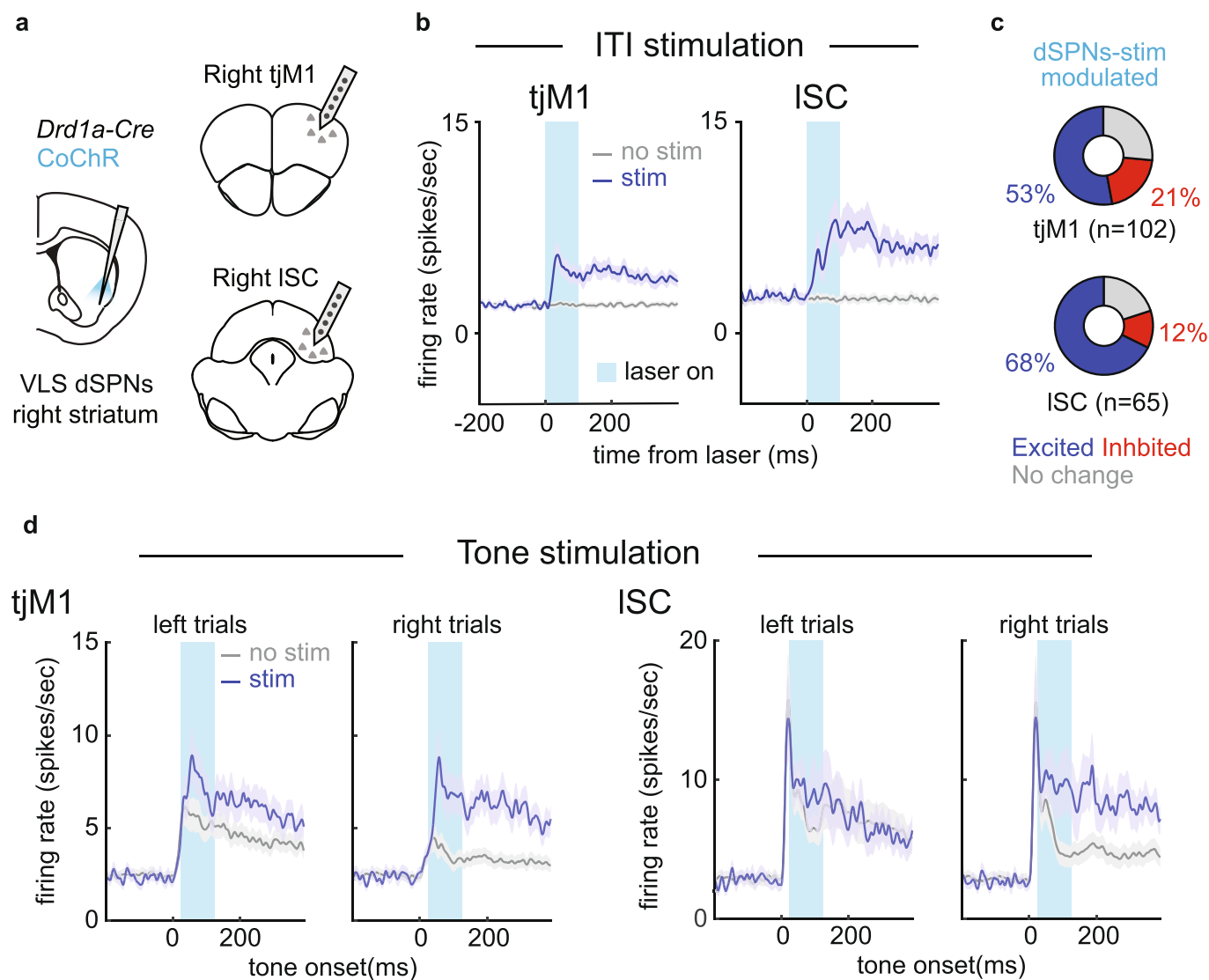
**Extended Data Fig. 7 | Anterogradely labelled putative dopamine axons in striatum.** **a**, Example coronal sections showing putative dopamine axons in striatum (from experiment described in Fig. 2e). Each row represent a distinct striatal injection of AAV1.cre from DMS, DLS and VLS. Injection site is shown in green (H2b-EGFP), dopamine axons in red (TdTom). For all three striatal injections, dopamine axons tend to co-localize with the injection site. Similar results were obtained in  $n = 9$  mice, 3 for each site. **b**, Schematic showing experiment for validating that the axons observed in striatum are dopamine axons. AAV1-Flpo was injected striatum, followed by a mixture of AAV-DIO-TdTom and AAV-Coff/Fon-EYFP in SNr/SNc, in a *Slc6a3-IRES-Cre* mouse, where Cre is expressed in dopamine neurons. This allowed us to anterogradely label SNr neurons, similar to experiment in Fig. 2e, but excluding the dopamine neurons (DA-/STR recipient), while also labelling dopamine neurons as a control. **c**, Example sagittal section showing the injection site. Dopamine neurons are expressing TdTom (red) whereas non-dopaminergic/anterogradely labelled cells are expressing EYFP (green). Similar results were obtained in  $n = 2$  mice. **d**, Sagittal sections showing axons in striatum (left), thalamus (middle) and SC (right). Dopaminergic axons (red:TdTom) were only seen in striatum, whereas non-dopaminergic/striatal recipient axon (green:EYFP) were only seen in thalamus and SC. Given the lack of EYFP fibers in striatum, axons seen in striatum from anterograde tracing at striatum (experiment in Fig. 2e) likely are dopamine axons. Similar results were obtained in  $n = 2$  mice.



**Extended Data Fig. 8 | SC projects back to Pf and VM in a topographical fashion.** **a**, Overlap of SNr axons labelled via anterograde tracing in striatum (AAV1.Cre, see Fig. 2e) and cortical axons. Scale bar, 500um. *bottom*, from Allen Institute for Brain Science. Allen Mouse Brain Connectivity Atlas (2011). Available from <https://connectivity.brain-map.org/>. **b**, Experimental protocol for labelling medial and lateral SC. Two anterograde tracers (AAV1.Cre and AAV1.Flpo) were injected in ACA/tjM1 respectively, followed by AAV.DIO.TdTom or AAV.fDIO.EYFP in medial or lateral SC. This allowed labelling of mSC and ISC without leaking into other regions outside SC. **c**, Example coronal section showing the injection site in SC (mSC in red, ISC in green). Similar results were obtained in  $n = 3$  mice. Scale bar, 1mm. **d**, Example coronal sections showing the axonal targets of mSC and ISC. We observed topography in both Pf and VM, similar to SNr topography (see main Text). Similar results were obtained in  $n = 3$  mice. Scale bar, 1mm.



**Extended Data Fig. 9 | Detailed optical setup for TF stimulation.** The optical setup allows depth dependent optical illumination combined with TF. The main components are: **P1**: pockel cell (or any power modulator), **S1**: shutter, **M1**: piezo mirror, **M3**: small mirror (0.5" diameter), **M2**: galvo mirror, **L1**: Achromatic doublet (AC508-200-A-ML,  $f=200\text{mm}$ , diameter 2", Thorlabs), **L2**: Aspheric condenser (ACL5040-A,  $f=40\text{mm}$ , diameter 50mm, Thorlabs), **X1**: XY translation cage mount + Z-axis translation mount (Thorlabs). M2 galvo mirror was used to change the incident angle onto the patchcord attached at the end of X1. M1 was used to correct for any misalignment for each angle.



**Extended Data Fig. 10 | dSPNs VLS stimulation engage cortical and collicular BG loops.** **a**, Schematic showing protocol for recording activity in tJM1 and ISC while stimulating VLS dSPNs. Mice were implanted with a single tapered fiber targeting VLS, and injected with AAV-DIO-CoChR in VLS, similar to experiment described in Fig. 6a (see methods). Extracellular recording with a silicon probe was done in tJM1 and ISC, on the same side (right hemisphere) as the stimulation side in striatum (n = 2 mice). **b**, Mean firing rate during the inter-trial-interval where mice were required to withhold licking, and during which VLS dSPNs stimulation caused contralateral licking (Fig. 6). Mean firing rate of both tJM1 (left) and ISC (right) increased during stimulation (blue, 100 ms stim) relative to no stimulation trial (grey). Shaded light blue represents laser on period (100ms) (n = 102 units in tJM1, n = 65 units in ISC) (mean  $\pm$  s.e.m across neurons). **c**, Fraction of cells that were significantly modulated by dSPNs stimulation in VLS in tJM1 (top) and SC (bottom). Cells are categorized into either excited (blue), inhibited (red) or no significant change (grey). The majority of cells recorded (53% in tJM1, 68% in ISC) were excited by the stimulation (0-500 ms window relative to laser onset,  $p < 0.05$ , Mann-Whitney U test, see Methods). **d**, Mean firing rate, during tone presentation, of cells that were significantly modulated during ITI stimulation. Firing rate for tJM1 (left) and ISC (right) in left trials and right trials. Firing rate during no stim (grey) and during stim trials (blue). Shaded light blue represents laser on period (100ms) (n=102 units in tJM1, n=65 units in ISC) (mean  $\pm$  s.e.m across neurons).

## Reporting Summary

Nature Research wishes to improve the reproducibility of the work that we publish. This form provides structure for consistency and transparency in reporting. For further information on Nature Research policies, see our [Editorial Policies](#) and the [Editorial Policy Checklist](#).

### Statistics

For all statistical analyses, confirm that the following items are present in the figure legend, table legend, main text, or Methods section.

n/a Confirmed

- The exact sample size ( $n$ ) for each experimental group/condition, given as a discrete number and unit of measurement
- A statement on whether measurements were taken from distinct samples or whether the same sample was measured repeatedly
- The statistical test(s) used AND whether they are one- or two-sided  
*Only common tests should be described solely by name; describe more complex techniques in the Methods section.*
- A description of all covariates tested
- A description of any assumptions or corrections, such as tests of normality and adjustment for multiple comparisons
- A full description of the statistical parameters including central tendency (e.g. means) or other basic estimates (e.g. regression coefficient) AND variation (e.g. standard deviation) or associated estimates of uncertainty (e.g. confidence intervals)
- For null hypothesis testing, the test statistic (e.g.  $F$ ,  $t$ ,  $r$ ) with confidence intervals, effect sizes, degrees of freedom and  $P$  value noted  
*Give  $P$  values as exact values whenever suitable.*
- For Bayesian analysis, information on the choice of priors and Markov chain Monte Carlo settings
- For hierarchical and complex designs, identification of the appropriate level for tests and full reporting of outcomes
- Estimates of effect sizes (e.g. Cohen's  $d$ , Pearson's  $r$ ), indicating how they were calculated

*Our web collection on [statistics for biologists](#) contains articles on many of the points above.*

### Software and code

Policy information about [availability of computer code](#)

**Data collection** Custom Matlab (2016b) code and Arduino code was used to collect data behavioral data and slice physiology data. OlyVIA 2.9/ImageJ1.46r was used to process and analyze histology data. FlyCapture2 was used to monitor behavior. OmniPlex1.16.1 was used to acquire Ephys data.

**Data analysis** Ethovision XT, Matlab (2016b) and Excel16.38 was used to analyze all data. Offline Sorter v3.3.5 was used to sort spikes for ephy data.

For manuscripts utilizing custom algorithms or software that are central to the research but not yet described in published literature, software must be made available to editors and reviewers. We strongly encourage code deposition in a community repository (e.g. GitHub). See the Nature Research [guidelines for submitting code & software](#) for further information.

### Data

Policy information about [availability of data](#)

All manuscripts must include a [data availability statement](#). This statement should provide the following information, where applicable:

- Accession codes, unique identifiers, or web links for publicly available datasets
- A list of figures that have associated raw data
- A description of any restrictions on data availability

The data that support the findings of this study are available from the corresponding author upon reasonable request.



## Field-specific reporting

Please select the one below that is the best fit for your research. If you are not sure, read the appropriate sections before making your selection.

Life sciences       Behavioural & social sciences       Ecological, evolutionary & environmental sciences

For a reference copy of the document with all sections, see [nature.com/documents/nr-reporting-summary-flat.pdf](https://www.nature.com/documents/nr-reporting-summary-flat.pdf)

## Life sciences study design

All studies must disclose on these points even when the disclosure is negative.

Sample size	No statistical methods were used to pre-define sample size. Our sample size are similar to previous studies (Kravitz, Tye and Kretizer, 2012) that have manipulated striatal activity using optogenetics.
Data exclusions	Based on our pre-defined criteria, animals in which the injection failed to label the correct striatal region were excluded for anatomical tracing (Fig. 1, 2). We also excluded animals in which we could not observe retrogradely labelled cells (from both populations) and CoChR expression in slice (Fig. 3d 4f).
Replication	We did not separately replicate the findings using new cohort of mice. However, we report all error bars, p-values for all our data, and our conclusion are based on statistically significant results.
Randomization	Optogenetic stimulation were randomly interleaved during the ITI and during trials(Fig. 6,7). Stimulation sites were also selected randomly during the session. We also randomized mice for all slice physiology experiments and all anatomy tracing experiments.
Blinding	For slice physiology, the experimenter was blind to the AAV1.Cre injection site (Fig. 3d, 4f). For other experiments, automated scripts were used to run all analysis.

## Reporting for specific materials, systems and methods

We require information from authors about some types of materials, experimental systems and methods used in many studies. Here, indicate whether each material, system or method listed is relevant to your study. If you are not sure if a list item applies to your research, read the appropriate section before selecting a response.

### Materials & experimental systems

n/a	Involved in the study
<input type="checkbox"/>	<input checked="" type="checkbox"/> Antibodies
<input checked="" type="checkbox"/>	<input type="checkbox"/> Eukaryotic cell lines
<input checked="" type="checkbox"/>	<input type="checkbox"/> Palaeontology and archaeology
<input type="checkbox"/>	<input checked="" type="checkbox"/> Animals and other organisms
<input checked="" type="checkbox"/>	<input type="checkbox"/> Human research participants
<input checked="" type="checkbox"/>	<input type="checkbox"/> Clinical data
<input checked="" type="checkbox"/>	<input type="checkbox"/> Dual use research of concern

### Methods

n/a	Involved in the study
<input checked="" type="checkbox"/>	<input type="checkbox"/> ChIP-seq
<input checked="" type="checkbox"/>	<input type="checkbox"/> Flow cytometry
<input checked="" type="checkbox"/>	<input type="checkbox"/> MRI-based neuroimaging

## Antibodies

Antibodies used	We used a Glial Fibrillary Acidic Protein (GFAP) antibody to stain for fiber tracts in striatum (Agilent Technologies, Z033429-2). Dilution of 1:500 was used.
Validation	The antibody has been validated by the company (see Instructions for Use, <a href="https://www.agilent.com/store/productDetail.jsp?catalogId=Z033429-2">https://www.agilent.com/store/productDetail.jsp?catalogId=Z033429-2</a> ).

## Animals and other organisms

Policy information about [studies involving animals](#); [ARRIVE guidelines](#) recommended for reporting animal research

Laboratory animals	All mouse handling and manipulations were performed in accordance with protocols approved by the Harvard Standing Committee on Animal Care, following guidelines described in the US National Institutes of Health Guide for the Care and Use of Laboratory Animals. For anatomical tracing, male and female Rosa26-Lox-STOP-Lox-H2B-EGFP and wild type (C57BL/6NCrI, Charles River) mice (age >P60) were used. For slice physiology, we used male wild type mice (C57BL/6NCrI, Charles River, age>P56). For behavioral experiments, we used Drd1a-Cre (B6.FVB(Cg)-Tg(Drd1-cre)EY262Gsat/Mmucd, 030989-UCD) on C57BL/6J backgrounds acquired from MMRRC UC Davis (age >P60). For in vivo validation of TFs, we used Adora2a-Cre (B6.FVB(Cg)-Tg(Adora2a-cre)KG139Gsat/Mmucd, 036158-UCD) from MMRRC UC Davis (age >P60). For dopamine axon validation experiment, male and female Slc6a3-IRES-Cre (age >P60) mice were used, obtained from the Jackson Laboratory (stock number 006660).
--------------------	---

Wild animals

our study did not involve wild animals

Field-collected samples

our study did not involve field-collected samples

Ethics oversight

All mouse handling and manipulations were performed in accordance with protocols approved by the Harvard Standing Committee on Animal Care, following guidelines described in the US National Institutes of Health Guide for the Care and Use of Laboratory Animals.

Note that full information on the approval of the study protocol must also be provided in the manuscript.